FEDERAL UNIVERSITY OF CEARÁ

CENTER OF SCIENCE

DEPARTMENT OF PHYSICS

POST-GRADUATION PROGRAM IN PHYSICS

MASTER DEGREE IN PHYSICS

ISIS DO VALE MEIRA LIMA

DETERMINATION OF VISCOELASTIC PROPERTIES OF LIVING CELLS FROM THE TIME-DEPENDENT INTERPRETATION OF HERTZ MODEL

FORTALEZA

2023

ISIS DO VALE MEIRA LIMA

DETERMINATION OF VISCOELASTIC PROPERTIES OF LIVING CELLS FROM THE TIME-DEPENDENT INTERPRETATION OF HERTZ MODEL

Dissertation submitted to the Post-Graduation Program in Physics of the Center of Science of the Federal University of Ceará, as a partial requirement for obtaining the title of Master in Physics. Concentration Area: Condensed Matter Physics.

Advisor: Prof. Dr. Jeanlex Soares de Sousa

FORTALEZA

2023

Dados Internacionais de Catalogação na Publicação
Universidade Federal do Ceará
Sistema de Bibliotecas
Gerada automaticamente pelo módulo Catalog, mediante os dados fornecidos pelo(a) autor(a)

L698d Lima, Isis do Vale Meira.
Determination of viscoelastic properties of living cells from the time-dependent interpretation of Hertz model / Isis do Vale Meira Lima. – 2023.
67 f. : il. color.

Dissertação (mestrado) – Universidade Federal do Ceará, Centro de Ciências, Programa de Pós-Graduação em Física, Fortaleza, 2023.
Orientação: Prof. Dr. Jeanlex Soares de Sousa.

1. Hertz Contact Theory. 2. Atomic Force Microscopy. 3. Nonlinear Effects. 4. Mechanical Properties. 5. Viscoelasticity. I. Título.

CDD 530

ISIS DO VALE MEIRA LIMA

DETERMINATION OF VISCOELASTIC PROPERTIES OF LIVING CELLS FROM THE TIME-DEPENDENT INTERPRETATION OF HERTZ MODEL

Dissertation submitted to the Post-Graduation Program in Physics of the Center of Science of the Federal University of Ceará, as a partial requirement for obtaining the title of Master in Physics. Concentration Area: Condensed Matter Physics.

Approved on: 24th August 2023

EXAMINATION BOARD

Prof. Dr. Jeanlex Soares de Sousa (Advisor)
Federal University of Ceará (UFC)

Prof. Dr. Cláudio Lucas Nunes de Oliveira
Federal University of Ceará (UFC)

Prof. Dr. Manfred Radmacher
Universität Bremen (UniBremen)

I dedicate this work to those who dreamed along with me and pushed me to make it happen.

ACKNOWLEDGEMENTS

Firstly, I would like to thank the Federal University of Ceará (UFC) for providing me with a productive environment, high-quality education, and excellent infrastructure, whether in the classrooms or advanced research laboratories. Secondly, I am grateful to the Postgraduate Program in Physics, the coordinators, secretaries, and the professors who instructed me during this important stage of the Academic Master's degree. This study was financed in part by the Coordenação de Aperfeiçoamento de Pessoal de Nível Superior – Brasil (CAPES) – Finance Code 001, with a scholarship from the Academic Excellence Program (PROEX).

In particular, I deeply thank Prof. Dr. Jeanlex Soares de Sousa for his excellent mentoring, respect, professionalism, and for all the support he has given to me since my undergraduate studies. You are the best. Words are not enough to express my gratitude. Here is something interesting: the other day, while I was studying German, I found myself wondering how to say "advisor" in that language. That was when I stumbled upon the perfect word to describe Prof. Jeanlex – *Doktorvater*, which is a combination of the words *Doktor* (doctor) and *Vater* (father). He worried about me like a father and was very demanding in research, just like a doctor, pushing me to reach new heights. Thank you for believing in my potential and helping me become who I am today.

To the invited professors who agreed to participate in the examining board, Prof. Dr. Cláudio Lucas Nunes de Oliveira and Prof. Dr. Manfred Radmacher, for their availability, valuable contributions, and suggestions to this work. I am also glad to Prof. Dr. Felipe Domingos de Sousa, from Núcleo de Biologia Experimental (NUBEX) at Universidade de Fortaleza (Unifor), who provided the cell culture studied in the present dissertation.

I would like to express my sincere appreciation to the members of the Biological Physics Laboratory at UFC for their tight unity, shared laughter (even during laboratory cleaning sessions with a soundtrack of cheesy songs), and unwavering support to each other. All of you possess remarkable talent, and I hold deep admiration for you: Thaís, Wallace, Vinnie, João, Edinaldo, Erick, Afonso, Damião, Dr. Rosemayre, and Alessandro.

Lastly, I am grateful to some very special people who have cared about me when I needed it, whether through priceless pieces of advice or comforting words: Rômulo Sampaio, Otávio Peixoto, Edinaldo de Oliveira, Thiago Alves, João Victor, Mrs. Jocyrrégia Peixoto, Lara Hissa, Isaac Taumaturgo, Renata Hora, and my little brother Lohan do Vale. Thank you for the support and for making me feel comfortable, even when I doubted myself.

"As long as the whole of the surface is not known to us, we shall let a definite discoverable point of the surface correspond to hardness, and be satisfied with finding out its position."

(HERTZ, 1896, p. 180)

ABSTRACT

In this master's thesis, we present a modified version of the Hertz contact theory, providing not only the elastic, but also the viscous characteristics of living cells. The Hertzian model imposes limitations when applied to complex scenarios involving larger deformations, non-ideal surfaces, and adhesive interactions. Despite its limitations, the Hertz model provides quick estimations and initial assessments of mechanical properties in a variety of experimental setups. However, when dealing with larger deformations, nonlinear effects, and adhesive interactions, more sophisticated models and techniques might be required to accurately understand the viscoelastic properties of biological samples. In this sense, conventional Hertz equation's Young's modulus is reformulated as a time-dependent function, enabling the analysis of the viscoelasticity. Thus, in order to prove our model experimentally, we used the atomic force microscopy (AFM) technique to explore the mechanical properties of L929 fibroblastic and OFCOL II osteoblastic cells. Furthermore, the proposed model was rigorously tested in various conditions, simulating different geometries of the indenter (conical, flat, and spherical), with minimal disparity of the estimated Young's moduli obtained from the power-law and Hertz models fitted to actual cell stiffness.

Keywords: Hertz contact theory; atomic force microscopy; nonlinear effects; mechanical properties; viscoelasticity.

RESUMO

Nesta dissertação de mestrado, apresentamos uma versão modificada da teoria de contato de Hertz, fornecendo não apenas as características elásticas, mas também as viscosas de células vivas. O modelo Hertziano impõe limitações quando aplicado a cenários complexos envolvendo deformações maiores, superfícies não ideais e interações adesivas. Apesar de suas limitações, o modelo de Hertz fornece estimativas rápidas e avaliações iniciais de propriedades mecânicas em uma variedade de configurações experimentais. Entretanto, ao lidar com maiores deformações, efeitos não lineares e interações adesivas, modelos e técnicas mais sofisticados podem ser necessários para compreender com precisão as propriedades viscoelásticas de amostras biológicas. Nesse sentido, o módulo de Young da equação convencional de Hertz é reformulado como uma função dependente do tempo, possibilitando a análise da viscoelasticidade. Assim, para comprovar experimentalmente nosso modelo, utilizamos a técnica de microscopia de força atômica (AFM), a fim de explorar as propriedades mecânicas das células fibroblásticas L929 e osteoblásticas OFCOL II. Além disso, o modelo proposto foi rigorosamente testado em diversas condições, simulando diferentes geometrias do indentador (cônico, plano e esférico), com disparidade mínima dos módulos de Young estimados obtidos a partir dos modelos power-law e Hertz ajustados à rigidez real da célula.

Palavras-chave: teoria do contato de Hertz; microscopia de força atômica; efeitos não lineares; propriedades mecânicas; viscoelasticidade.

LIST OF FIGURES

LIST OF TABLES

LIST OF SYMBOLS

d	Deflection of the cantilever
z	Position of the cantilever relative to the sample surface
δ	Indentation
t	Time
F	Force
k	Spring constant
x	Amount of extension
σ	Stress
ε	Strain
E	Young's modulus
A	Area
f	Frequency
Δl	Deformation
l_0	Initial length
τ	Shear stress
γ	Shear strain
G	Shear modulus
ν	Poisson's ratio
μ	Viscosity
De	Deborah number
λ_r	Time of relaxation
T	Time of observation

CONTENTS

1 INTRODUCTION

The Hertz contact theory is widely used to obtain rheological information from biological samples, being originally developed for elastic materials without considering viscosity. Regardless of this limitation, many researchers choose to use the Hertz model due to its simplicity and ease of implementation. In this context, our work aims to advance scientific knowledge by studying and characterizing the microrheology of living cells through a modified Hertz model. Our modified model incorporates a time-dependent Young's modulus, allowing us to obtain viscoelastic information and explore the nonlinear viscoelastic regime of cells. Thus, by investigating the microrheological properties of living cells, we gain valuable insights into their structure, function, and mechanical interactions. Therefore, this study provides a comprehensive understanding of the complex behavior of living cells under varying mechanical forces and dynamic changes, with significant implications for regenerative medicine, cell therapies, and the comprehension of cell mechanics in health and disease.

In Chapter 2 of this thesis, we have a theoretical framework with biological arguments about the biomechanics of living cells, focusing on animal eukaryotic cells, which were substantial for the investigation developed in this work. We then clarify the mechanical functions performed together by three main components involved in cell mechanics: cytoskeleton, extracellular matrix, and cell junctions. These structures gain prominence among the other cellular components, as they interact with each other, affecting their microrheological properties. Throughout this chapter, we further address the historical development of Rheology and the relevance of the Microrheology to comprehend biological systems. Moreover, as will be better explained later, we will see that Microrheology consists of a set of active and passive techniques, such as magnetic tweezers, microfluidic filtration, cytometry, atomic force microscopy, among others. Particularly, we used an atomic force microscope (AFM) in this study, approaching about the Hertz contact theory and how it is related with the Boltzmann's Superposition Principle.

In Chapter 3, we describe in detail the materials and methods adopted to measure the microrheological properties of two different cell lines: L929 (fibroblast cells) and OFCOL II (osteoblastic cells). Initially, we will present the specifications of the atomic force microscope and the cantilever used for contact mode force curve measurements. In addition, we will briefly describe the main calibrations to be performed on the equipment so that it works properly and we can obtain more accurate results. Then, we will perform the cell culture protocol according to established guidelines.

Finally, in Chapter 4, we will present the theoretical model proposed to describe the microrheological properties of living cells, taking into account the experimental results obtained. Our theoretical model seeks to fill the gap left by the Hertz model, incorporating the effects of viscosity in the rheological calculations of living cells. We also show detailed experimental results, including stress-strain curves, modulus of storage and loss, and statistical analysis of the obtained data. These results provide a deeper understanding of the microrheological properties of L929 fibroblasts and OFCOL II osteoblasts, contributing to the development of the field of biomechanics, paving the way for future research and clinical applications.

2 THEORETICAL FRAMEWORK

This chapter focuses on providing a physical understanding of the biomechanics of living cells. Firstly, we will discuss the biological mechanisms that enable relaxation and contraction of cells to fully comprehend their complex mechanical behavior. In this context, we will consider the role of cellular tensegrity, which involves the interplay between the cytoskeleton, the extracellular matrix, and the cell junctions. Secondly, our investigation will delve into the application of various cellular microrheology techniques. In this way, we will elucidate the valuable insights and data that can be extracted from each technique, while also acknowledging their inherent limitations. Lastly, we will make an explanation about the linear viscoelasticity theory, specifically in the context of nanomechanical characterization of biosamples, focusing on Hertz Contact Theory and Boltzmann's Superposition Principle. To summarize, by providing a detailed analysis of these fundamental concepts and techniques, this chapter aims to enhance the readers' understanding of the biomechanics of living cells.

2.1 Biomechanics of living cells

Considered the fundamental unit of life, the cell (from the Latin word *cella*, which means "small chamber", reminiscent of chambers in a monastery) was first observed by the British scientist Robert Hooke (1635-1703). In his influential work "Micrographia" published in 1665, Hooke used a compound microscope of his own design to examine a thin slice of cork under magnification. This allowed him to observe small box-like structures with empty spaces that showed a similarity to miniature chambers, as depicted in **Figure 1**. This discovery was a milestone in the history of biology, as it established the existence of basic structural units in living organisms. Subsequently, other scientists such as Matthias Schleiden and Theodor Schwann contributed to the development of the cell theory, giving rise to the field of Cytology.

Currently, living cells can be categorized into two primary groups: prokaryotes and eukaryotes. This classification is determined by the presence or absence of a nucleus that is surrounded by a nuclear membrane, effectively separating the genetic material from the cellular cytoplasm. Represented by bacteria and cyanobacteria, prokaryotic cells are simpler and more primitive, not possessing a true nucleus, i.e., their genetic material is dispersed in the cytoplasm. On the other hand, eukaryotes encompass cells from the Animalia, Plantae, Fungi, and Protista kingdoms, possessing a distinct nucleus where the genetic material is dispersed.

Figure 1 – Drawing made by Robert Hooke to describe the cell wall of cork cells based on his observations of the *Quercus suber* plant, known as the cork oak. In this plant, Hooke was able to visualize and describe the cellular structures that make up the cork.

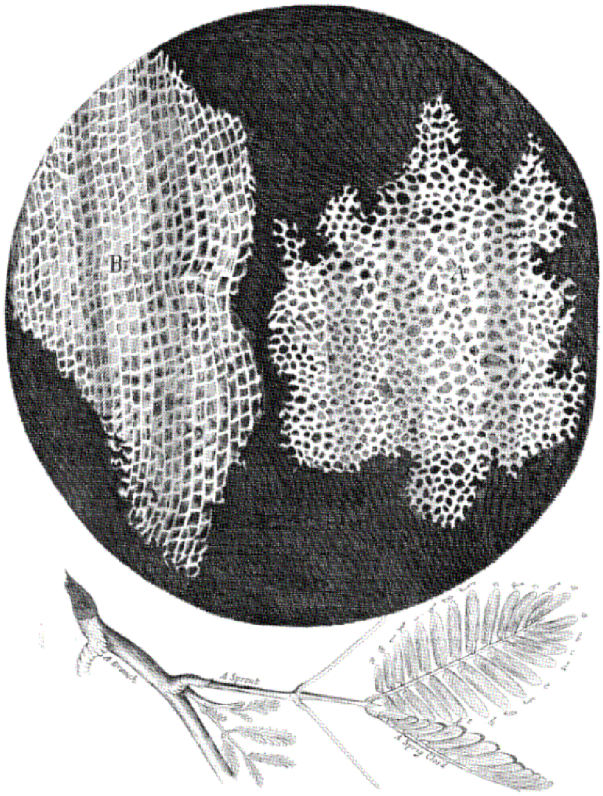

Source: (HOOKE, 1665, p. 114).

Over the past few decades, research in the field of cellular biomechanics has made significant progress, rapidly advancing our understanding of the mechanics of living systems, with a wide range of biophysical, physiological, and medical applications. In this study, our focus will be on exploring the biomechanical properties of different lineages of animal eukaryotic cells among the vast array of cell types. Keeping this in mind, it is crucial to develop physical and mathematical models that assist us in explaining the mechanics of cells and tissues, as well as how their adhesion can affect cell stiffness. This will expand our understanding of differentiation, diseases, and mutations. The main cellular components responsible for responding to mechanical stresses applied to the cell surface are the cytoskeleton, the extracellular matrix, and the cell junctions, as will be clarified in the following sections.

2.1.1 Cytoskeleton

As shown in **Figure 2**, the cytoskeleton of eukaryotic cells consists of three main semiflexible filaments: actin filaments, intermediate filaments, and microtubules, which are arranged in a worm-like chain (WLC) configuration.

Figure 2 – Schematic representation of the cellular cytoskeleton: actin filaments (in red), intermediate filaments (in purple), and microtubules (in green), highlighting the structural components of the cytoskeleton.

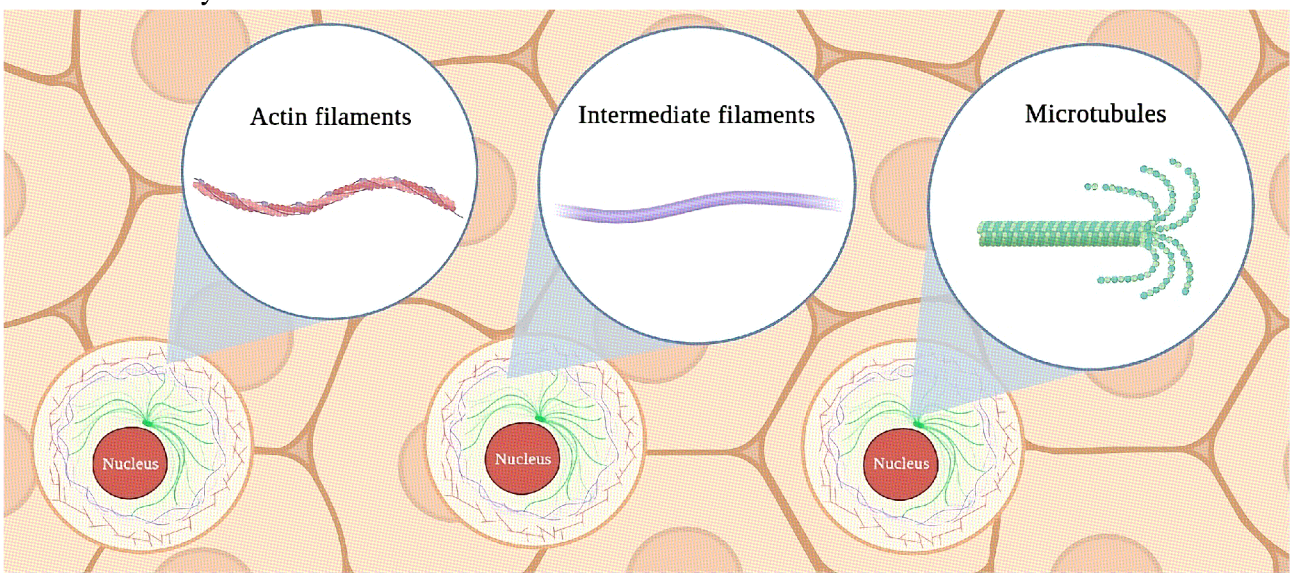

Source: Created by the author with BioRender.

2.1.1.1 Actin filaments

Commonly situated in the cortex and near the cell membrane's outer edges, the actin filaments are considered the thinnest among the other filaments that compose the cytoskeleton, which is why they are also known as microfilaments. The diameter of these filaments can range from 6 to 8 nanometers. Their structure is composed of actin monomers, referred to as G-actin, which is a globular protein characterized by its compact and three-dimensional shape. These monomers tend to associate in a preferred orientation, ensuring the polarity of the resulting double helical filament called F-actin, as illustrated in **Figure 3**. The helical shape is typically achieved through the association of actin filaments with fragments of the myosin molecule, resulting in arrowhead-like ends. This polarization leads to a faster process of F-actin polymerization with a greater attraction of G-actin monomers at the barbed end (+). Conversely, the pointed end (-) tends to remove monomers more rapidly, promoting depolymerization. Despite this, when actin filaments are associated with stabilizing proteins, they can also adopt a more stable form.

Among the various mechanical functions of the cell performed by the actin-myosin filament network, we can highlight: cell shape and cell movement, interactions with membrane receptors, and formation of the contractile ring during cell division. This filamentous tangle constitutes the actin cortex and plays a vital role in certain dynamic processes such as endocytosis, exocytosis, cell adhesion, and cellular protrusion expansion. Moreover, cellular locomotion

Figure 3 – Formation of double helical F-actin structure from the G-actin monomers. It is possible to observe the barbed end (+) attracting a greater amount of monomers, while the pointed end (-) displays a higher rate of monomer removal.

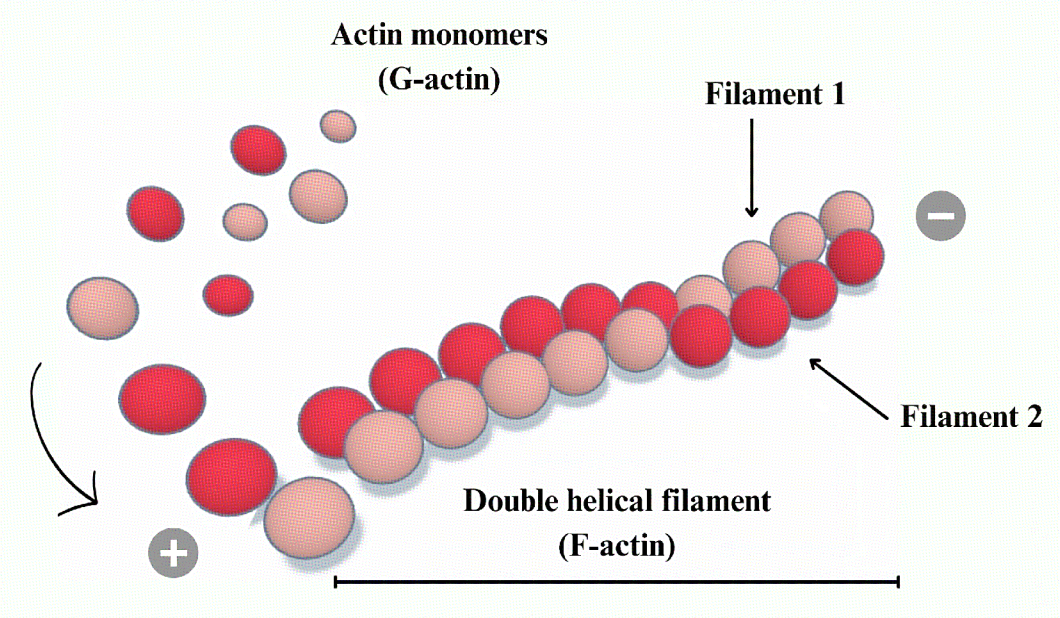

Source: Created by the author.

on solid substrates is only possible through the establishment of specialized contact regions between the cell and the extracellular matrix. This is facilitated by the generation of contractile forces, the presence of internal cellular stress (known as prestress), and the association of these phenomena with traction movements. Consequently, as the cytoskeleton experiences consecutive substrate adhesion and readaption to the surrounding environment, certain structures enable the extension of the cytoplasm in the direction of movement, as exemplified in **Figure 4**. This, in turn, effectively displaces the cell. In more detail, what happens is the polymerization of microfilaments, which propels the plasma membrane forward, allowing the formation of protrusions called lamellipodia due to their blade-like shape.

Another relevant aspect worth mentioning is the impact caused by the alterations to the cytoskeleton due to the presence or absence of gelsolin in the actin cortex. Gelsolin is an accessory protein responsible for sequestering actin monomers. Additionally, when gelsolin is activated by binding to Ca^{+2}, it can also induce the shortening and fragmentation of the actin filament it binds to. This nomenclature stems from the direct association between gelsolin and cytoplasmic phase transitions known as the gel (denser and more viscous) and sol (more fluid) states. This occurs because when actin filaments are shortened, the cytoplasm becomes more liquefied, while in contrast, an increased quantity of actin filaments results in a more solidified

cytoplasmic environment.

Figure 4 – Representation of cell movement and the role of actin filaments: (1) Microfilament polymerization with the induction of lamellipodium protrusive extension. (2) New adhesions are formed due to the membrane extension. (3) Then, contractile forces produced by stress fibers generate tension, allowing cell body movement. (4) The de-adhesion process takes place as a transition from strong adhesions to weak local adhesion to the substrate. As the cell retracts its edge, old adhesions enter an intermediate state of adhesion without the presence of tension fibers (GREENWOOD; MURPHY-ULLRICH, 1998).

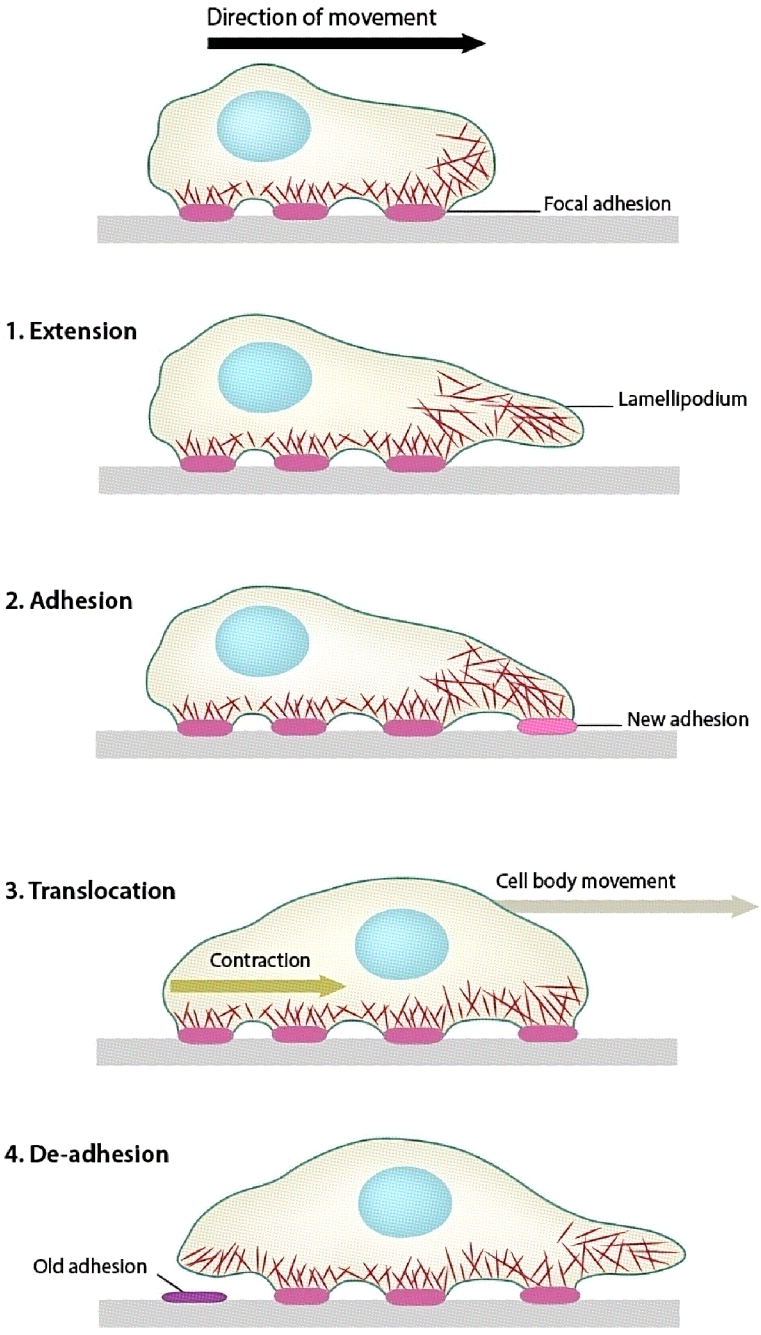

Source: (MECHANOBIOLOGY INSTITUTE , 2018).

2.1.1.2 Intermediate filaments

Intermediate filaments, unlike microfilaments, are not composed of globular proteins, but rather more than 50 different types of fibrous proteins, such as keratins, desmin, vimentin, among others. This association of mostly polymerized proteins confers the formation of coiled-coil structures, which exhibit high mechanical resistance to traction forces. The name "intermediate" is attributed to the fact that these filaments have an average diameter, ranging from 8 to 12 nanometers, when compared to microfilaments and microtubules. In addition, as the intermediate filaments do not have polarity, they guarantee greater stability to the cytoskeleton, even contributing to the anchoring of cellular organelles.

2.1.1.3 Microtubules

Microtubules are composed of monomers of the globular protein tubulin, which form a dimer of two similar polypeptide chains called α and β tubulins through a strong binding. They are approximately cylindrical and hollow, with the largest diameter among the filaments that make up the cytoskeleton, ranging from 22 to 24 nanometers. These tubulin dimers are dispersed throughout the cytoplasm and organize themselves in an oriented manner, generating polarization of the microtubules, which allows for the directed transport of different structures along them. Within the cell, microtubules perform a variety of essential functions, such as determining cell shape, organizing the cytoplasm, and being responsible for the transport of vesicles and organelles. Thus, during cell division, microtubules are crucial for chromosome separation. These structures are highly dynamic as they can continuously polymerize and depolymerize, adjusting to the cell's needs in terms of intracellular transport and structural reorganization.

2.1.2 Extracellular matrix and the elastic fiber system

The extracellular matrix (ECM) can be understood as a three-dimensional network of macromolecules responsible for filling the intercellular spaces, mainly composed of proteins and carbohydrates. This complex of macromolecules tend to associate in a way that forms a set of different structures, allowing us to subdivide the ECM into three categories: fibrillar components, non-fibrillar components, and microfibrils, as described in **Figure 5**.

The first one, called **fibrillar components**, consists of fibrillar collagens and elastic fibers. They may contribute to the proper function of tissues in response to mechanical stresses

Figure 5 – Illustration of the components of the extracellular matrix, which consists of a network primarily composed of proteins, such as collagen fibers, and carbohydrates.

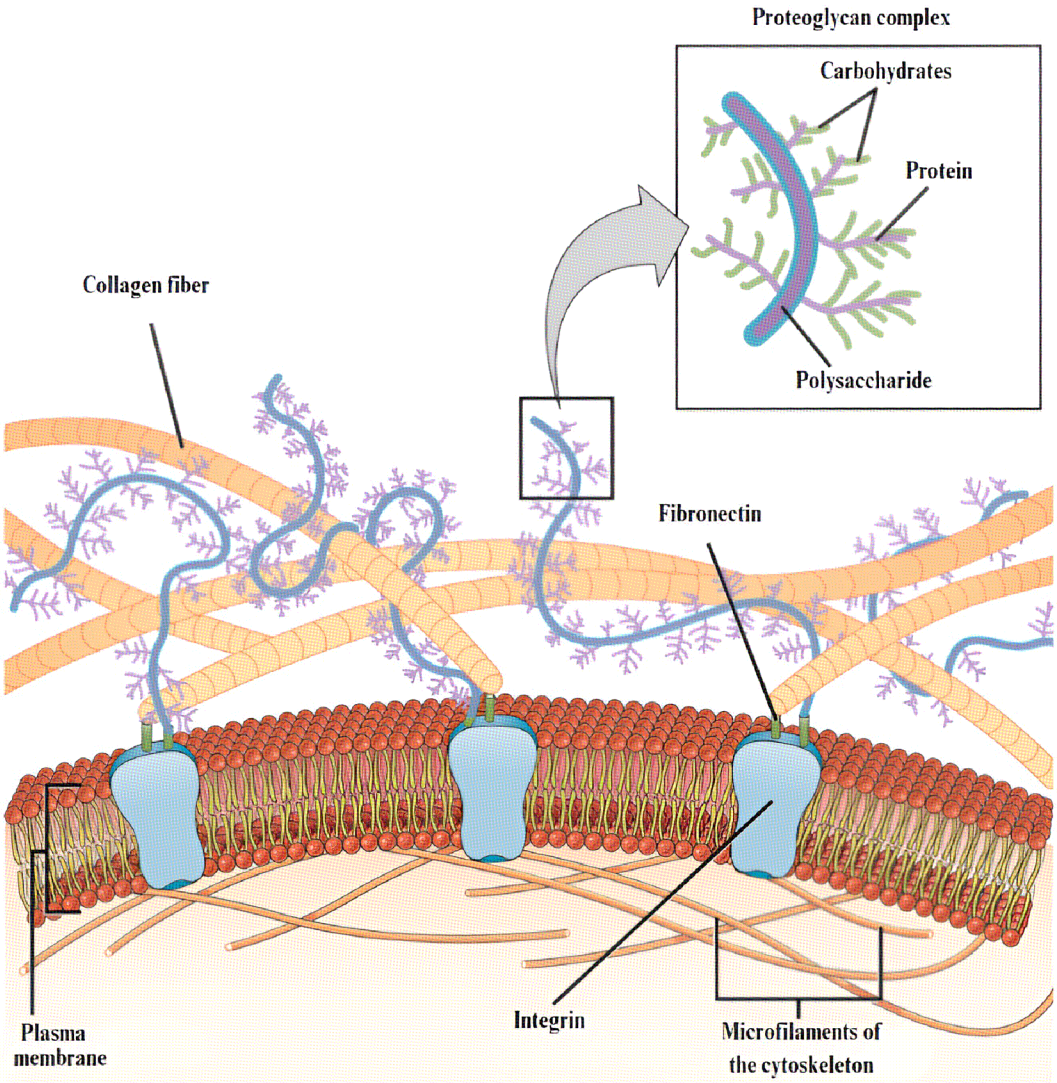

Source: (CLARK *et al.*, 2018, p. 118).

and strains. While fibrillar collagens form long and fibrous structures that provide strength and structural support to various tissues, elastic fibers, on the other hand, are specialized components that provide elasticity and retraction properties to tissues.

The second category, know as **non-fibrillar components**, includes proteoglycans (PGs), i.e., protein molecules that contain carbohydrates, and the group of non-collagen structural glycoproteins. On the one hand, proteoglycans consist of a central protein linked to long and unbranched carbohydrate chains called glycosaminoglycans (GAGs). These elongated GAG chains give proteoglycans their viscous and gelatinous properties and play an important role in compressive strength, maintenance of hydration, and regulation of the cellular environment. In contrast, glicoproteins are proteins to which shorter and less complex carbohydrate chains

are attached. Glicoproteins have several functions, including cell recognition, cell adhesion, molecular transport, and cellular signal transduction.

The last group encompasses the **microfibrils**, which are composed of collagen type VI (ColVI) and elastin proteins. ColVI forms complex networks that give strength and support to tissues, while elastin gives remarkable flexibility and elasticity that facilitates stretching and subsequent recovery from deformation. Together, these two proteins contribute to the overall integrity and functionality of tissues, ensuring that they can withstand mechanical stress and maintain their optimal performance.

Thus, among these categories of macromolecules, there are two proteins that are directly related to the elastic properties of the ECM, namely elastin and fibrillin. Jointly, they form the elastic fiber system, which has been given this name because of its spring-like behavior and its ability to deform and return to its original shape without expending energy.

Figure 6 – Cycle of retraction and distension of the elastic fiber system.

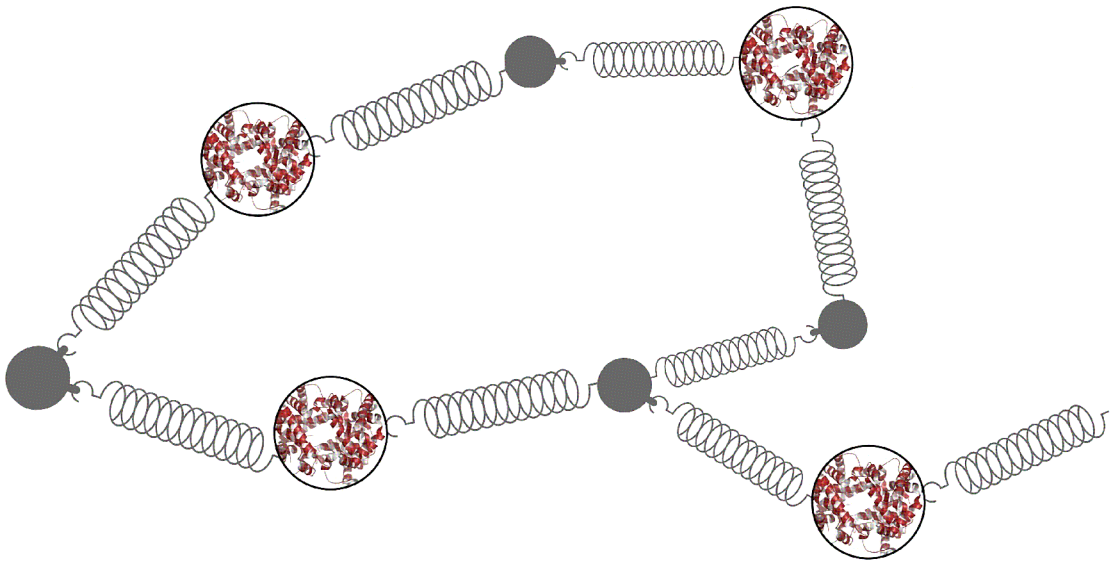

Source: Created by the author.

Figure 6 illustrates how the elastin molecules rearrange themselves in the elastic fiber system during the retraction and distension cycle. Furthermore, because elastin is not a water-miscible protein, it tends to organize itself into small hydrophobic domains, forming internal amino acid structures (in red) that are separated from the hydrophilic region. Nevertheless, when these hydrophobic domains experience deformation forces, the system tends to return to an equilibrium state in accordance with Hooke's law. As a result, the amino acids exposed to the surrounding aqueous environment reassemble, leading to the retraction of the entire ensemble,

thus shortening the elastic fiber system.

2.1.3 Cell junctions

Cell junctions are specialized structures distributed along the plasma membrane that perform several functions, including facilitating adhesion and nutrient exchange between cells (known as intercellular junctions) and between cells and the extracellular matrix (known as cell-matrix junctions). However, it is important to emphasize that not all animal cells have cell junctions, as is the case with red blood cells. Additionally, it has been observed that certain medical conditions, such as bacterial infections, cancer, and metastasis, are directly correlated with defects in specific cell junctions. Hence, comprehending the biological arguments concerning the mechanical properties of these structures and their simultaneous interaction with the cytoskeleton and the ECM allows us to approach a field of knowledge that bridges the gap between physics and biology.

2.1.3.1 Cell-cell junctions

Intercellular junctions are responsible for allowing connections between neighboring cells within a tissue, as is the case with epithelial tissue. According to Elisabetta Dejana, these junctions not only allow adhesion, but also transfer signals that help control apoptosis (programmed cell death, PCD, caused by the activation of enzymes that degrade the cell's DNA and proteins), in addition to regulating the formation of blood vessels (DEJANA, 2004). Moreover, by considering their specific functions, there are four types of cell-cell junctions: occlusion junction, adherent junction, desmosome, and communicating junction, which will be more detailed further below in **Figure 7**.

Also known as zonula occludens or tight junction, the **occlusion junction** has a characteristic shape that resembles a belt that surrounds a cell. The main role of this junction is to act as a diffusion barrier, which tends to control the permeability of substances that come into contact with the cell, such as ions, H_2O, and other molecules.

Similar to the occlusion junction, the **adherent junction**, also known as zonula adherens, encircles the cell like a ring around the apical boundaries of neighboring cells. It receives this name because it provides cell attachment mediated by the presence of cadherin and catenin proteins. Whereas cadherins are transmembrane adhesion proteins that mediate cell adhesion, catenins are cytoplasmic proteins that bind to cadherins and help transmit the adhesion

signal to actin filaments of the cytoskeleton. As observed in the literature, most tumor cells have low adhesion to other cells, which results in greater motility and uncontrolled growth of transformed cells (SOUSA *et al.*, 2020). Consequently, the maintenance of adherent junctions directly affects the triggering of the tumor and the metastasis process.

Figure 7 – Schematic representation of the intercellular junctions that are present in the plasma membrane of most animal eukaryotic cells. At the top of the image, we have several cells interacting with each other by contact forming a monolayer. At the bottom, when we enlarge the region of contact between two adjacent cells, we can observe the different cell-cell junctions.

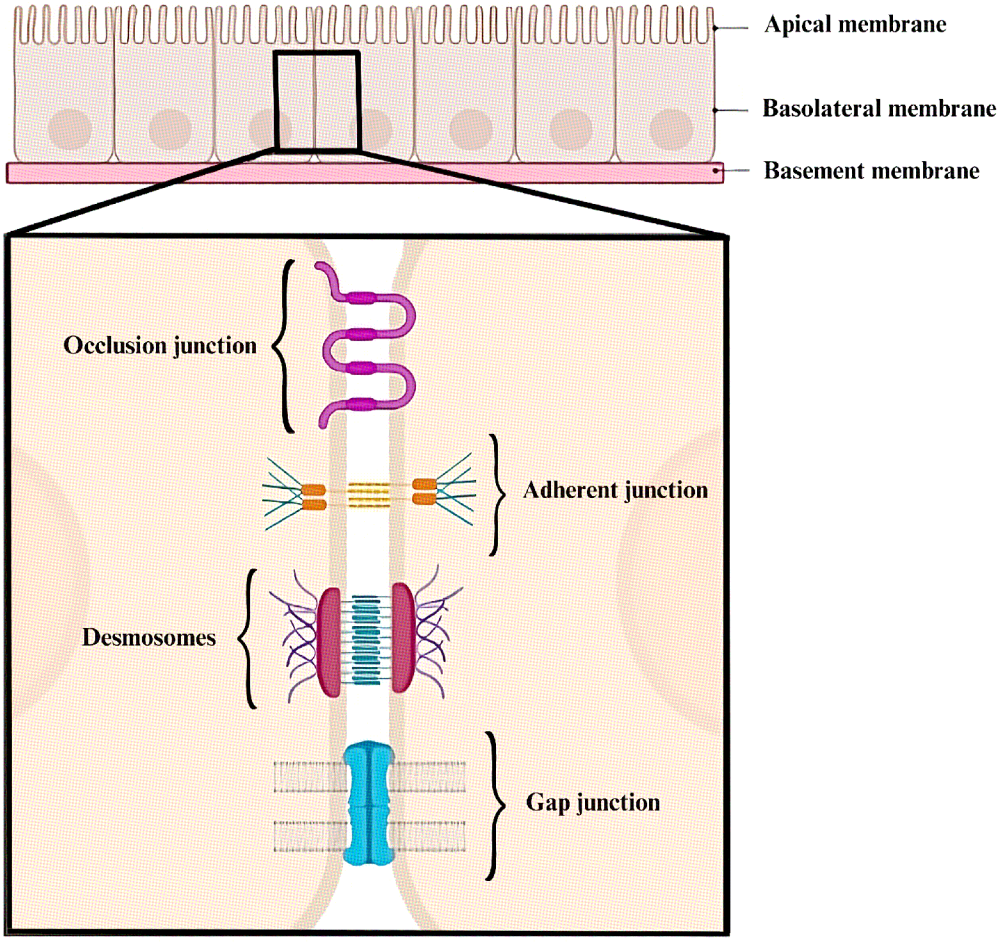

Source: Created by the author with BioRender.

Present in many tissues, such as epithelial, breast and cardiac tissue, **desmosomes** are composed of transmembrane proteins, like desmogleins and desmocholins, which bind to one another across contiguous cells. Also referred to as maculae adherens, these junctions are associated with intermediate filaments via a network that connects all of the desmosomes spread throughout the plasma membrane (GARROD; CHIDGEY, 2008). This association leads to structures that effectively resist mechanical stress, with desmosomes being recognized as

hyper-adhesive intercellular junctions.

Found in many kinds of cells, including bone, cardiac, and vascular cells, the **communicating junction**, often referred to as nexus or gap junction, promotes the connection between the cytoplasm of two adjacent cells. Its structure, formed by a series of channels, allows the passage of electrical current and nutrient exchange. Moreover, its valve-like dynamics that open and close can be influenced by external mechanical forces, while they play an important role in regulating cell growth and differentiation (SALAMEH; DHEIN, 2013).

2.1.3.2 Cell-matrix junctions

As important as the intercellular junctions are, the cell-matrix junctions enable the adherence and interaction of the cell with the ECM through adhesion molecules embedded in the plasma membrane, as depicted in **Figure 8**. Based on this, we can classify cell-matrix junctions into two categories: hemidesmosome and focal adhesion junction, which will be clarified in the next paragraphs.

Figure 8 – On the left side, we have a cell culture, where cells are adhered to a substrate. The substrate typically consists of the extracellular matrix (ECM) or a surface designed to imitate ECM properties. On the right side, we see a magnified image of the region of contact between the cell and the ECM, showing the cell-matrix junctions: hemidesmosomes and focal adhesion.

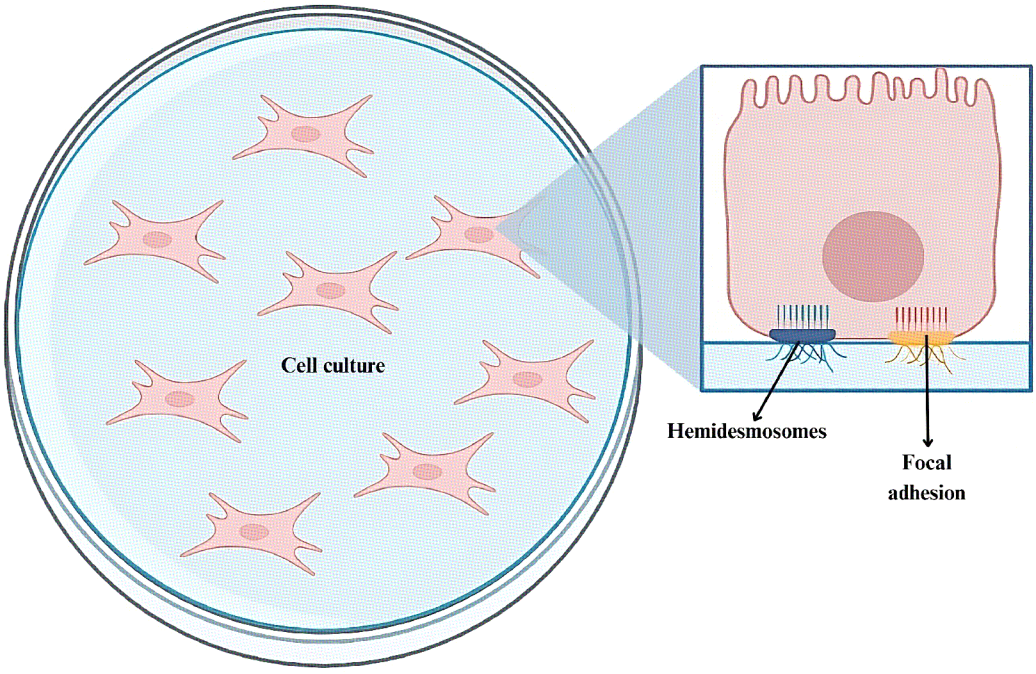

Source: Created by the author with BioRender.

Hemidesmosomes (HD), considered multiprotein complexes, are responsible for connecting the ECM with the intermediate filaments of the cytoskeleton, which confers resistance to mechanical stresses. From the Greek, *hemi* means one-half, and *desmos* means ligament. Therefore, we can infer that HD are structures similar to half of a desmosome (WALKO *et al.*, 2015). However, despite this ultrastructural similarity, HD are composed of proteins different from those that constitute desmosomes, the so-called integrin proteins.

Like hemidesmosomes, **focal adhesions junctions** (also known as adhesions plaques or focal contacts) are made up of transmembrane proteins integrins, which act as nutrient receptors of the extracellular matrix, among other substances that have growth and differentiation factor (BURRIDGE *et al.*, 1988). These structures were first observed using the electronic microscopy technique, due to an increase in electron density in these regions of the plasma membrane (ABERCROMBIE *et al.*, 1971). Furthermore, there is an association of cytoskeletal microfilaments with focal adhesion junctions, resulting in the formation of stress fibers. These fibers allow cell adhesion to rigid substrates and, consequently, anchorage-dependent cell growth, with regulated growth control through apoptosis, which is not observed in tumor cells.

2.1.4 Microrheology of biological systems

In the 1920's, Eugene Cook Bingham (1878–1945), professor and head of the department of chemistry at Lafayette College, published his pioneering work in which he defined Rheology as *the study of the deformation and flow of matter* (BINGHAM, 1929; BARNES *et al.*, 1989). This was a landmark in the beginning of a broad understanding of the behavior and properties of materials subject to deformation or tension, such as elasticity, plasticity, viscosity and flow (BARNES, 2000). With the advancement of this highly interdisciplinary science, Rheology aims to comprehend the deformability of soft materials, including foams, polymers, gels, colloids, as well as most soft biological materials (cells, tissues, and organoids).

Moreover, as previously stated, it was possible to qualitatively delineate that cells indeed exhibit mechanical properties characteristic of each lineage. These properties can be affected by external forces or genetic mutations in specialized structures that can trigger the tumor process. Therefore, by considering cells as physical entities, we can analyze this system from a mechanical perspective, in particular, within the interdisciplinary area of Microrheology — a specific domain within the broader field of Rheology (CICUTA; DONALD, 2007).

This approach enables us to present quantitative arguments associated with the

understanding of mechanical models for living cells and their applications. Taking this into account, here is a formidable definition of microrheology according to Cicuta and Donald (2007, p. 1449):

> Microrheology is a term that does not describe one particular technique, but rather a number of approaches that attempt to overcome some serious limitations of traditional bulk rheology, such as the range of frequency and moduli that can be probed, the sample size and heterogeneity, and cost. The "micro-" in the term refers to the size of the stress/strain probe, which is typically a micron-sized colloidal particle, but also indicates that this type of rheology can be carried out on very small volumes, of the order of a micro-litre.

Based on the above definition, we will discuss the two main classes of microrheological techniques (see Table 1): active methods and passive methods. While active methods encompass techniques that involve active manipulation of probes by applying local stress, passive methods are those that measure passive particle movements due to thermal or Brownian fluctuations (ASHEGHI *et al.*, 2005).

Table 1 – Microrheological techniques most widespread among scientists in the study of mechanical properties of living cells, classified as active and passive methods.

Microrheological Techniques	
Active methods	Passive methods
Magnetic Tweezers	Particle Tracking Microrheology (PTM)
Optical Tweezers	Diffusing Wave Spectroscopy (DWS)
Optical Stretcher	Dynamic Light Scattering (DLS)
Microfluidic Filtration	
Real Time Deformation Cytometry (RT-DC)	
Atomic Force Microscopy (AFM)	

Source: Created by the author.

2.1.4.1 Active microrheological techniques

Firstly, in **Figures 9a** and **9b**, we briefly present the physical principle of Optical Tweezers (also known as optical trapping or laser tweezers), which was developed by Ashkin and colleagues in 1986. This method uses laser light focused on the object to be manipulated to obtain mechanical measurements of biological materials such as cells and proteins (ASHKIN *et al.*, 1986). Nevertheless, optical traps have a limitation concerning cell microrheology, especially when considering the maximum force that can be applied without damaging the sample—approximately a hundred piconewtons (MIERKE, 2018). As a result, employing core-shell particles becomes necessary to apply forces on the order of nanonewtons, as reported by Zhong *et al.* (2014).

Secondly, considered one of the oldest biological nanomanipulation techniques, Magnetic Tweezers are well-known for incorporating magnetic particles into a sample and subjecting it to an external magnetic field. **Figure 9c** provides a schematic representation of the experimental setup regarding this approach, showing the magnetic stage with four coils and the microscope objective. As mentioned in the work of Mao *et al.* (2022), when spherical beads are attached to the sample, they act as microscopic probes that can be manipulated using an external magnetic field. This configuration induces deformations in the material, actively measuring the force response and, hence, its mechanical properties, particularly the rheological behavior at microscale (ASHEGHI *et al.*, 2005).

Figure 9 – In (a), we have a illustration with the main physical concepts of Optical Trapping technique. The laser beam refracts the light rays as they interact with a spherical sample. Then, a photograph (b) was taken using a green-blocking filter to image red fluorescence in water, improving the visibility of incident and scattered beam trajectories. In contrast, (c) shows a schematic illustration of the apparatus configuration, depicting how the Magnetic Tweezers work.

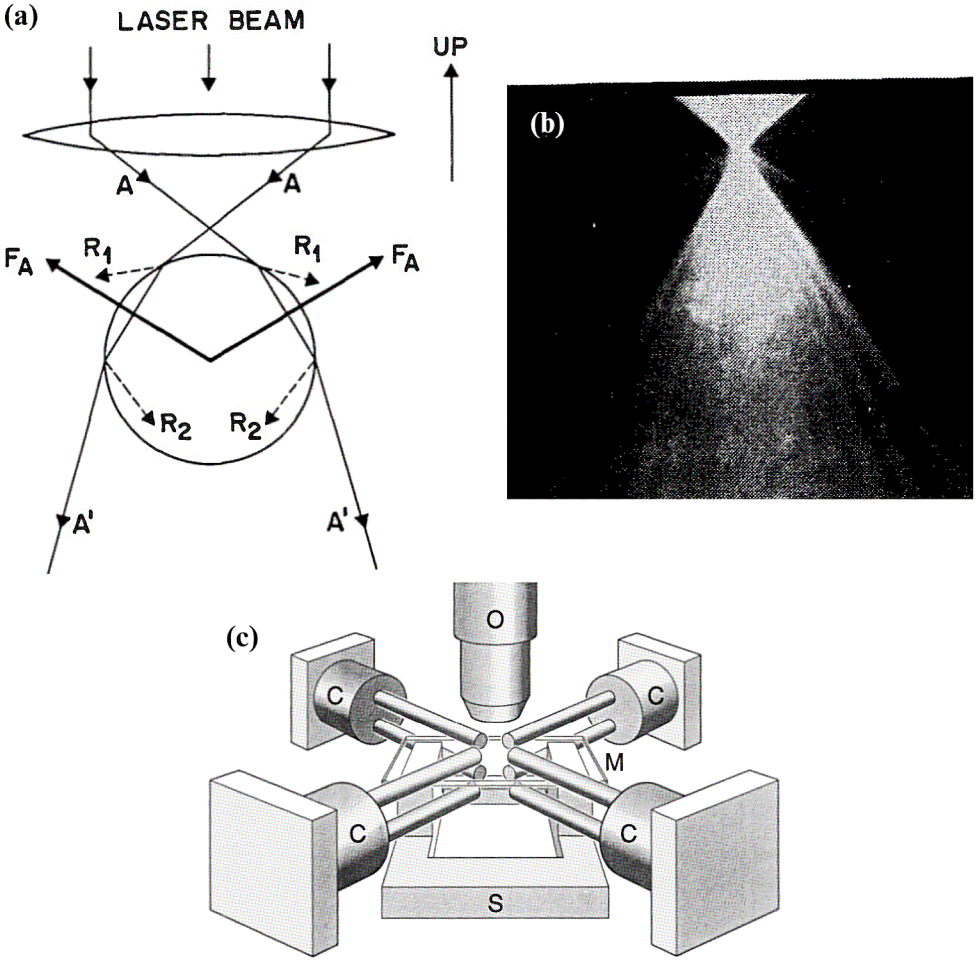

Source: (ASHKIN *et al.*, 1986; AMBLARD *et al.*, 1996).

Thirdly, with a similar principle to the techniques described above, the Optical Stretcher is a highly useful device in the study of mechanical properties of suspended cells during measurement, as exemplified in **Figure 10**. In this technique, two opposing divergent lasers are directed at the same cell (GUCK *et al.*, 2001). When both beams reach equal intensity, the resulting force acting on the cell cancels out along the optical path. From this, it is possible to obtain time-dependent deformation curves of the cell, which can be fitted with rheological models to extract the viscous and elastic contributions of these materials.

Figure 10 – Experimental set-up and principles involved in the Optical Cell Stretcher technique.

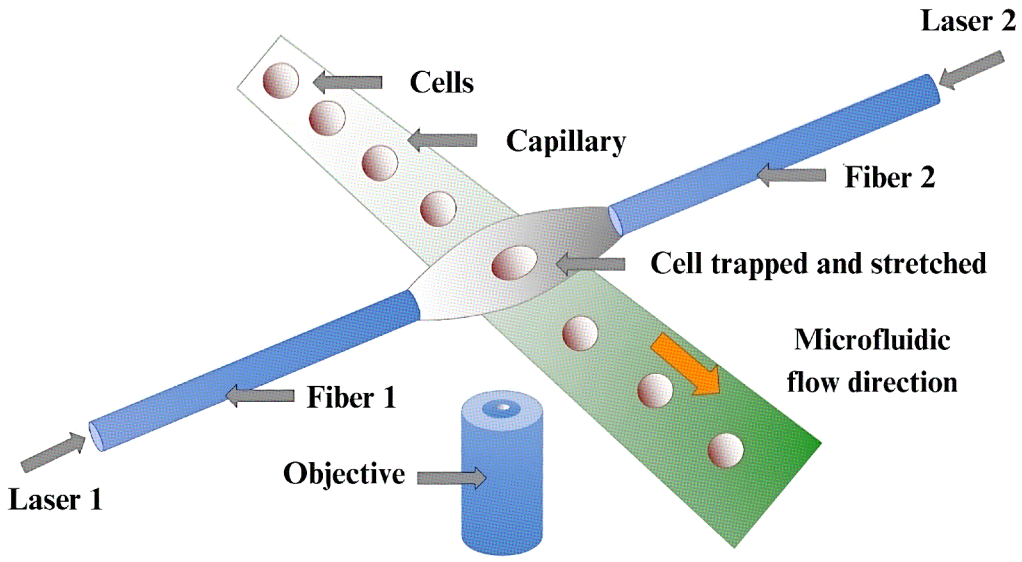

Source: (MIERKE, 2018, p. 3-16).

Another approach is Microfluidic Filtration, which considers deformable cells can pass through pores or microfluidic channels more easily than rigid cells. Based on that, fabrication methods such as soft lithography are commonly used to create multiple microchannels in chips made of PDMS (polydimethylsiloxane). This allows researchers to create microchannels with sub-micrometer and nanometer-scale features (MIERKE, 2018). An example of its use is the study of hemodynamics, in which microchannels mimic blood vessels and even allow the study of the metastasis process (OMORI *et al.*, 2014). Thus, in a single system, it is possible to group regions with different functions, similar to what occurs *in vivo*. Therefore, cell deformability is assessed by measuring the pressure required for a given sample to pass through a constriction in a microfluidic channel, in accordance with **Figure 11**.

Similarly to the previous technique, Real-Time Deformation Cytometry (RT-DC) stands out as a sensitive microfluidic method used to measure cell stiffness. It enables mechanical

Figure 11 – The device design comprises four functional regions: an entry port, a cell filter, constricted channels, and an exit port. When enhancing the resolution in the constricted channel area, we can observe the precise architecture in regions as narrow as $10\mu m$, indicated by the scale bar.

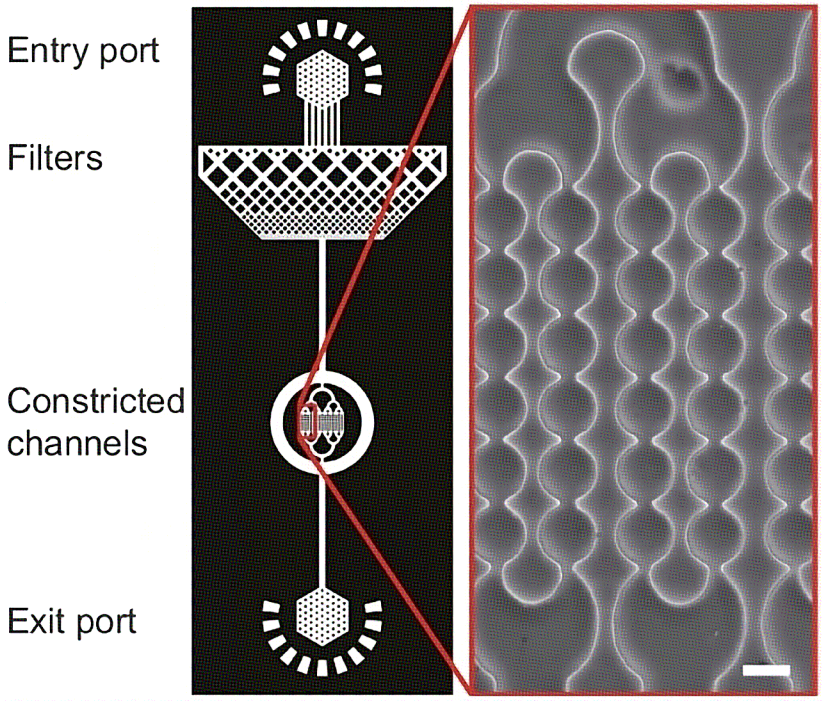

Source: (HOELZLE *et al.*, 2014).

characterization of numerous continuous cells from extensive populations (over 100,000 cells), with the capacity to analyze more than a hundred cells per second in experiments (OTTO *et al.*, 2015). **Figure 12** shows that RT-DC deforms cells using only hydrodynamic interactions, since there is no contact with the walls of the channels through which they flow. Moreover, this cell deformation occurs due to the high velocity gradients that exist in the channel's cross-section (MIERKE, 2018, p. 3-32). RT-DC measurements are performed using a highly controlled microfluidic process. First, the cells are individually encapsulated in microdroplets in a low viscosity solution and inserted with a syringe into a microfluidic channel. These microdroplets are then deformed by mechanical forces precisely applied along the channel. As cells undergo these controlled deformations, high-sensitivity sensors capture their mechanical responses in real time. Based on the collected data, it is possible to calculate the stiffness and other mechanical properties of the cells, providing a detailed understanding of the biological and mechanical characteristics of a large population of cells in a short period of time.

Lastly, we have the Atomic Force Microscopy (AFM), reported for the first time by Binnig *et al.* (1986). AFM was developed to address the challenges of studying non-conducting

Figure 12 – Illustration of the Real-Time Deformation Cytometry (RT-DC) experiment procedure.

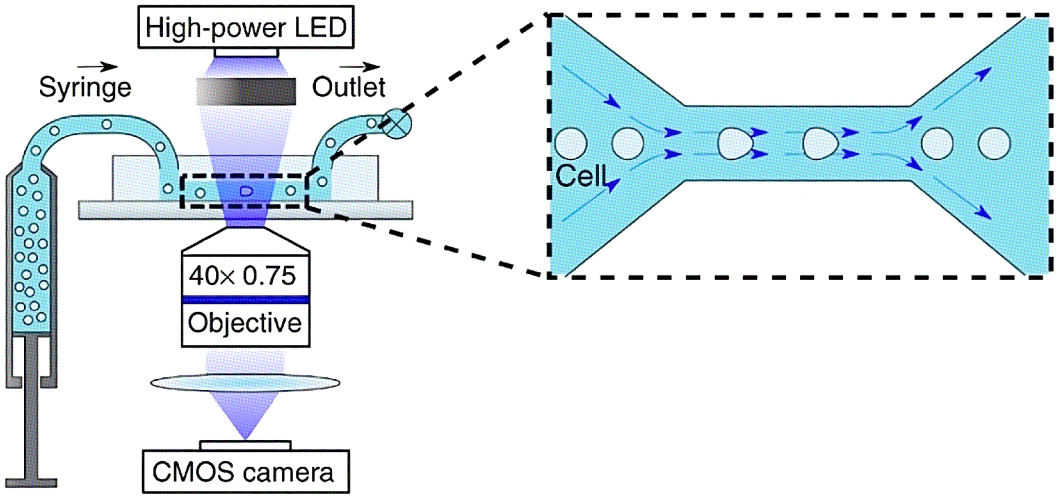

Source: (OTTO *et al.*, 2015).

materials with a less invasive approach, such as biological samples. Despite the term "microscopy", this technique has a different principle from conventional methods of obtaining high resolution images, not using light or electrons, as is the case with optical and electron microscopes, respectively. Instead, the AFM is based on the principle of measuring the deflections of a cantilever subject to intermolecular attractive and repulsive forces resulting from the interaction with the sample (ZANETTE, 2010).

Furthermore, we can operate this microscope in different modes, including tapping mode, non-contact mode and contact mode. This technique is not limited to obtaining images of the topography of the materials because it also enables the application of forces of the order of nanonewtons to the surface of the materials, thus measuring their rheological properties. As stated by Flormann *et al.* (2021), it is important to mention that there are several protocols for the application of these external forces on the samples, the main ones being: (i) stress relaxation, (ii) creep compliance, and (iii) oscillatory tests.

2.1.4.2 Passive microrheological techniques

As reported by Asheghi *et al.* (2005, p. 18), passive microrheological techniques refer to approaches that leverage the Brownian dynamics of embedded colloids for assessing the material's rheology and structure. Notably, Particle Tracking Microrheology (PTM), Diffusing Wave Spectroscopy (DWS), and Dynamic Light Scattering (DLS) are prominent methods within

this category. An advantage regarding the PTM is that it enables the tracking of thermally driven motion with high precision, measuring the mechanical response inside the cytoplasm of a cell, without requiring direct contact between the cell and an external probe (MOEENDARBARY; HARRIS, 2014). This non-invasive characteristic makes it a valuable tool for studying cellular properties and behavior, facilitating the mimicking of three-dimensional physiological conditions.

On the other hand, DWS and DLS are two techniques that utilize light scattering to investigate complex fluids and materials, including cell microrheology. In DWS, for example, a laser beam is directed at an opaque sample, and the light interacts with scattering elements in the sample. The propagation of the light through the sample is mathematically described by the diffusion equation (ASHEGHI *et al.*, 2005). This technique provides valuable information about the dynamics of the scattering elements, allowing scientists to explore the movement and interactions of particles in a sample. In contrast, DLS is a method that has a limitation in studying only transparent samples in order to occur the refraction phenomena (MAO *et al.*, 2022). Despite this, the DLS allows extracting not only the viscosity, but also the modulus of elasticity of a viscoelastic material by measuring the temporal correlation function of the scattered light.

2.1.4.3 Constitutive relationships: stress and strain

In accordance with the previous section, we inferred that microrheological techniques provide experimental data that can be used to validate, refine and even derive constitutive equations that describe the physical response of a material at the microscale. The constitutive relationships relate stress and strain, providing a mathematical framework to understand and predict the mechanical behavior of materials under applied forces (PHAN-THIEN, 2002). It is known that materials respond differently to compressive, tensile, and shear forces, resulting in distinct modes of deformation. The elastic modulus and shear modulus represent the material's stiffness and its response to normal and shear forces, respectively, as shown in **Figure 13**. Furthermore, cells exhibit both elastic and viscous properties, making them known as viscoelastic materials. Thus, to provide a clearer understanding of these concepts, we will now explore the Hookean elastic solid and the Newtonian viscous fluid.

Elasticity is a physical property observed when a material is subject to reversible deformations, i.e., it returns to its equilibrium state after ceasing the tension acting on it. An example that illustrates this is when we exert a force on a spring, either by compressing or stretching it. Then, if exactly after we release the ends of the spring, it recovers its original length

without the need for additional external forces, this demonstrates that the elastic energy had been stored, emphasizing its elastic property. On other hand, if the material exceeds its elastic limit and cannot return to its original length, it exhibits plastic behavior. Based on that, we can define Hookean elastic solids as materials governed by Hooke's law:

$$\mathbf{F} = -k\mathbf{x}, \tag{2.1}$$

where **F** is the restoring force (or applied force), k is the spring constant, and **x** is the amount of extension. However, Equation 2.1 is traditionally used in contexts involving springs or mechanical systems and expresses that *extension is proportional to the force* (PHAN-THIEN, 2002, p. 60). Therefore, from a broader point of view, we can express Hooke's law in a more general form, as follows:

$$\sigma = E\varepsilon, \tag{2.2}$$

where σ represents the normal stress, E is the Young's modulus (also known as modulus of elasticity), and ε is the normal strain (TAYLOR, 2013). The main advantage of writing Hooke's law as shown in Equation 2.2 is that the modulus of elasticity E is independent of material dimensions, unlike the spring constant k. In this context, the normal stress can be defined as the force exerted on a surface, which can be interpreted as pressure:

$$\sigma = \frac{F}{A}. \tag{2.3}$$

Conversely, strain is a dimensionless quantity that characterizes the change in shape or size of a material in response to an applied stress. It measures the magnitude of deformation Δl experienced by the material relative to its original size l_0, defined as:

$$\varepsilon = \frac{\Delta l}{l_0}. \tag{2.4}$$

In addition to normal forces, acting perpendicular to the surface of a material, it is also relevant to consider the case where tangential forces are applied. An analogous way of expressing Equation 2.2 is to consider the constant called shear modulus, G, through the following linear constitutive relationship:

$$\tau = G\gamma, \tag{2.5}$$

where τ is defined as the shear stress and γ represents the shear strain, quantified as a shift in the angle between lines that were initially perpendicular. In this case, deformation can be

represented by the shear angle, α, which corresponds to the angular rotation between parallel lines in a material before and after the application of shear forces, as follows:

$$\tau = G\tan\alpha. \tag{2.6}$$

Moreover, it is worth mentioning that the shear modulus is related to Young's modulus through the following equation:

$$G = \frac{E}{2(\nu+1)}. \tag{2.7}$$

In Equation 2.7, we are faced with the Poisson's ratio, ν, which was well-marked according to Tschoegl *et al.* (2002) as:

> (...) an elastic constant defined as the ratio of the lateral contraction to the elongation in the infinitesimal uniaxial extension of a homogeneous isotropic body. In a viscoelastic material Poisson's ratio is a function of time (or frequency) that depends on the time regime chosen to elicit it. It is important as one of the material functions that characterize bulk behavior.

In simpler words, the Poisson's ratio quantifies the extent to which a material contracts or expands in perpendicular directions to the applied stress. Moreover, in the work by Malvern (1969), it was clearly demonstrated that the value of this parameter is directly influenced by the atomic and molecular structure of the material, in addition to the physical properties and its chemical composition, in a range of $-1 \leq \nu \leq 0.5$. A positive ratio indicates that a material tends to contracts in the transverse direction when stretched axially, while a negative ratio indicates that the material expands in the transverse direction. In the case of soft materials such as living cells, it is considered that $\nu \approx 0.5$ because they have a lower capacity for lateral deformation when compared to other materials.

Almost a decade after Hooke's work on elasticity, the English physicist and mathematician Isaac Newton (1642-1727) first addressed the concept of viscosity, which he initially explained as a *lack of slipperiness*. Nowadays, the science dedicated to the study of viscosity is called Viscometry (BARNES, 2000). When we want to quantify a material's ability to resist flow under an external force, we are interested in measuring the viscosity of materials. Thereby, this physical property refers to a fluid's resistance to shear flow and can be determined by the ratio of shear stress to shear strain rate, as following:

$$\tau = \mu\dot{\gamma} \implies \mu = \frac{\tau}{\dot{\gamma}}, \tag{2.8}$$

Figure 13 – Representation of the physical quantities (a) stress and strain, when a material is subjected to normal or tangential stress. (b) The static mechanical properties of a material are characterized by the stress-strain relationship. (c) Soft materials exhibit a linear relationship between stress and strain during small deformations. Nonetheless, as deformations become larger, the stress-strain relationship becomes nonlinear, with stress increasing at a more rapid rate.

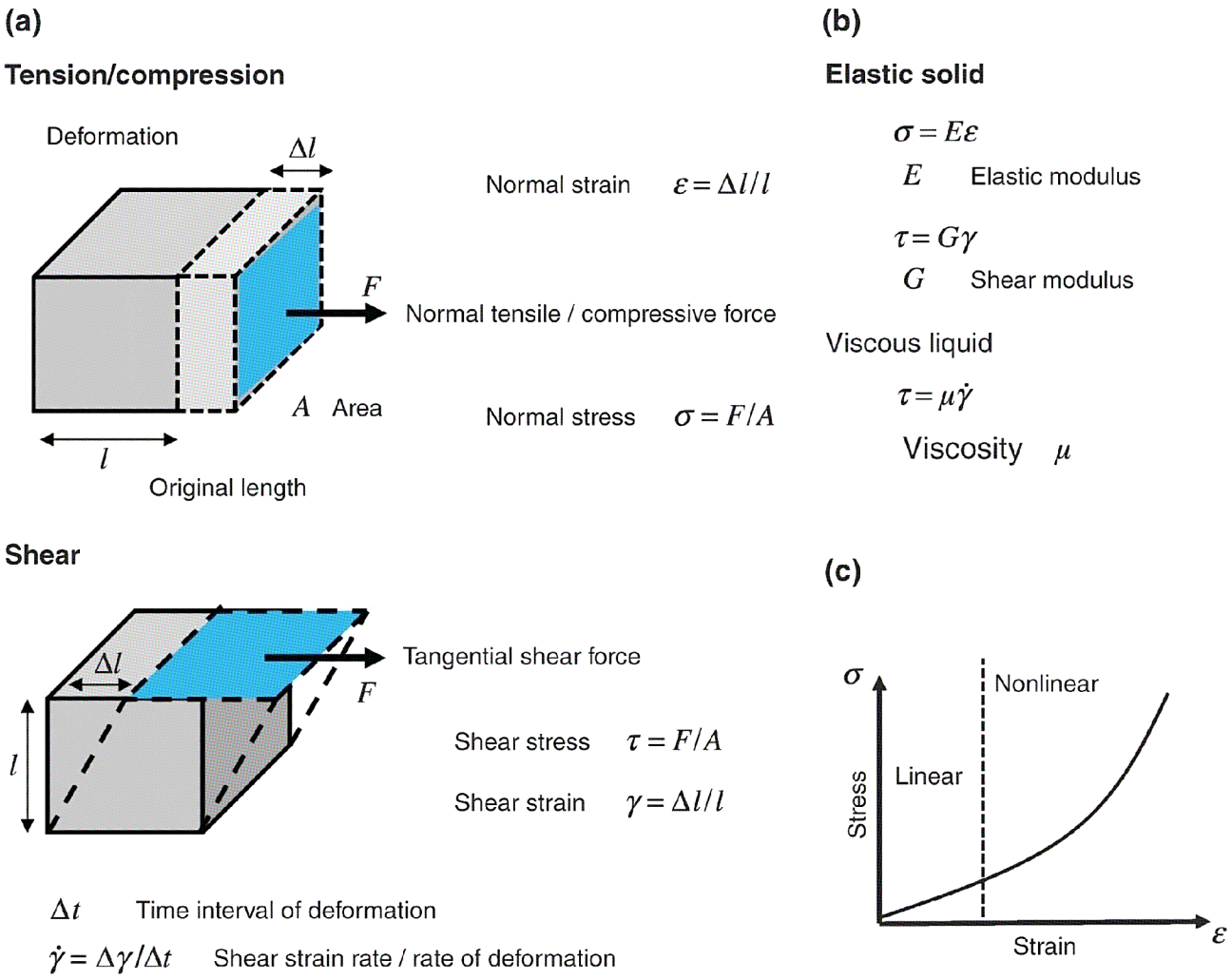

Source: (MOEENDARBARY; HARRIS, 2014).

where μ is the viscosity constant.

From Equation 2.8, we can observe a linear relationship between the shear stress and the shear strain rate, which is characteristic of Newtonian viscous fluid. However, it's important to recognize that many fluids in nature deviate from this linear behavior for not having a homogeneous viscosity. In more complex materials, such as those with viscoelastic properties, constitutive relationships may involve additional parameters related to nonlinear behavior (KOLLMANNSBERGER; FABRY, 2011). These relations describe the time-dependent or nonlinear responses of the materials under stress and strain.

2.2 Linear viscoelasticity: springs and dashpots

Linear viscoelasticity refers to the rheological behavior of materials exhibiting elastic (spring-like) and viscous (damper-like) properties. The spring represents the elastic component, storing energy during deformation and exhibiting a reversible response, while the damper represents the viscous component, dissipating energy during deformation and exhibiting a time-dependent response (MOEENDARBARY; HARRIS, 2014). Hence, viscoelasticity can be effectively modeled using combinations of springs and dampers.

Despite that, Lakes (1998) stated in his book *Viscoelastic solids* that in order to have a broader understanding of the viscoelastic properties of materials, we cannot limit ourselves to describing circuits formed by a small number of springs and dampers. Indeed, it is essential to recognize that materials encompass a range of distinct timescales. This means that their behavior is better understood through the lens of more complex configurations of springs and dampers, combined both in series and in parallel. This aligns with the idea of the Boltzmann superposition principle, where the relaxation behavior of a material is considered to be the result of a combination of various relaxation mechanisms operating on different timescales. This reformulation produces relaxation moduli composed as a combination of exponential functions, each with a separate relaxation time as a parameter.

2.2.1 Deborah number

Given the birth of Rheology, Bingham became aware of the work reported by Markus Reiner (1886-1976), a civil engineer from Israel who dedicated himself to researching the flow of plastic materials. Consequently, in 1928, Reiner was invited to work at Lafayette College, where he made significant contributions from this collaboration (REINER, 1964). One of them was the rheological characterization of the materials from the Deborah number, De, a dimensionless quantity defined by the ratio between the relaxation time, λ_r, which represents the time spent for a material to return to its undeformed state after applying a force, and the time of observation, T, which is the time taken to apply a deformation, as expressed in the equation below:

$$De = \frac{\lambda_r}{T}. \tag{2.9}$$

Furthermore, this fundamental number of rheology can be understood based on the following statement made by Reiner (1964):

> The difference between solids and fluids is then defined by the magnitude of De. If your time of observation is very large, or, conversely, if the time of relaxation of the material under observation is very small, you see the material flowing. On the other hand, if the time of relaxation of the material is larger than your time of observation, the material, for all practical purposes, is a solid.

In order to comprehend the Equation 2.9, it is essential to bear in mind that the macromolecules of a material always tend to return to their equilibrium state (PHAN-THIEN, 2002, p. 63). Initially, in **Figure 14a**, we have an example of an elastic solid material thrown (I) towards the ground, suffering an elastic collision with the surface (II), which causes material deformation. After the collison, (III) the material returns to its original shape almost immediately after the applied force is removed. This enables us to affirm that a material has a solid-like response when $\lambda_r > T$, i.e., the experiment time tends to be very small..

Figure 14 – Examples of materials characterized by the Deborah number. In (a), we have an example of an elastic solid ($De \to \infty$), represented by a sphere made of a natural rubber, allowing the material to quickly return to its original shape after deformation. Moreover, (b) shows a viscous fluid ($De \to 0$), such as honey, with the applied deformation maintained over time.

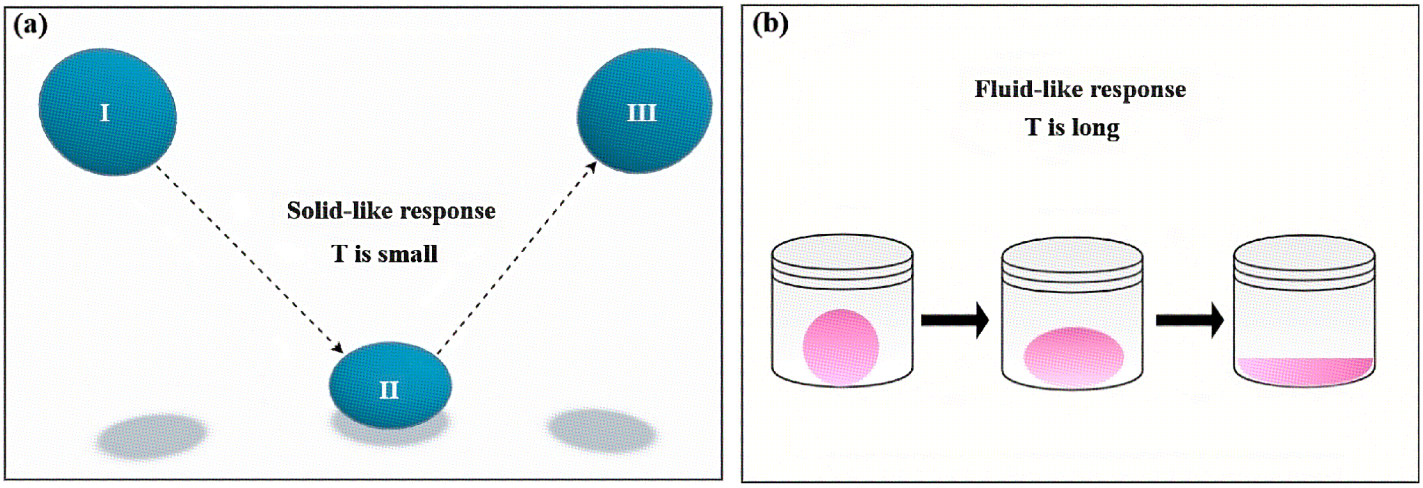

Source: Created by the author.

On the other hand, **Figure 14b** displays the behavior of a viscous fluid. We deduced that materials with this property are affected by the effect of a sustained deformation over time. This is because molecular chains have a hard time getting back to their original configuration quickly. Therefore, a material exhibits a fluid-like response when $\lambda_r < T$, i.e., the fluid relaxation time tends to be smaller than the time of observation.

3 MATERIALS AND METHODS

3.1 Atomic Force Microscopy

In the present work, the experiments were performed with an MFP-3D atomic force microscope integrated with an inverted microscope, manufactured by Asylum Research (Digital Instruments, Santa Barbara, CA). The AFM is shown in **Figure 15**. Moreover, we used PNP-TR-Au type probes, which stands for Pyrex-Nitride Probe, with triangular-shaped cantilevers that were gold (Au) coated on the pyramidal tip side. The cantilevers were made of silicon nitride (Si_3N_4), fabricated by NanoWorld Innovative Technologies, with nominal spring constant measured of $k = 0.08$ N/m and resonance frequency of $f = 17$ kHz.

Figure 15 – Experimental setup images before starting the data acquisition. (a) MFP-3D-BIO AFM used in this study operating in liquid contact mode. (b) Properly positioned cell culture sample in a Petri dish on the equipment. After that, to initiate our measurements, the cantilever was duly placed on the head (c) and submerged in the cell culture liquid.

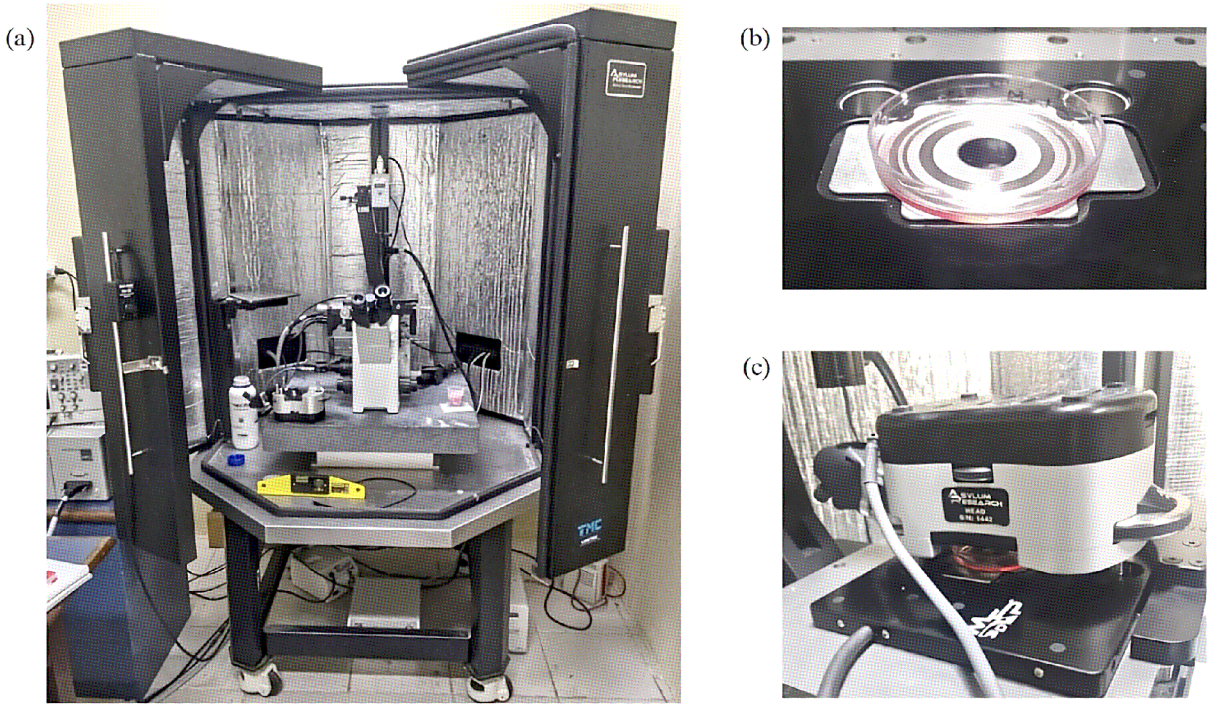

Source: Created by the author.

Acquiring sample force curves in contact mode requires following the calibration protocol of the device. From this protocol, we can obtain the cantilever spring constant, k, an essential parameter in the AFM feedback system and, consequently, in the control of mechanical movements performed by piezoelectric ceramics. Also, it is interesting to mention that the

corrections to be discussed need to be done only once, regardless of whether we change the medium (air or liquid) afterwards.

In order to eliminate possible instrumental errors, the first step is to correct the virtual deflection. The term virtual deflection refers to a mechanical coupling between the movement along the z axis and the cantilever deflection signal. It intrinsically depends on the mechanical path, which tends to undergo a slight inclination in the force curve. This correction ensures that distortions do not occur in the accuracy of measurements and in the analysis of rheological data.

Finally, we measure the inverse optical lever sensitivity (InvOLS) from the thermal power spectral density, which consists of the cantilever vibrating in air and on an ideally hard sample (clean glass slide) to determine the cantilever resonance frequency. Then, knowing the resonance frequency, we apply a certain force to the cantilever and measure the corresponding deflection, obtaining the InvOLS value, as depicted **Figure 16**. In this way, InvOLS computes

Figure 16 – Representation of the inverse optical lever sensitivity measured from a force curve on a hard surface. The OLS is the ratio of the signal from cantilever deflection in volts (blue vertical line) to the nanometer displacement in z (green horizontal line). Hence, InvOLS is the inverse of OLS.

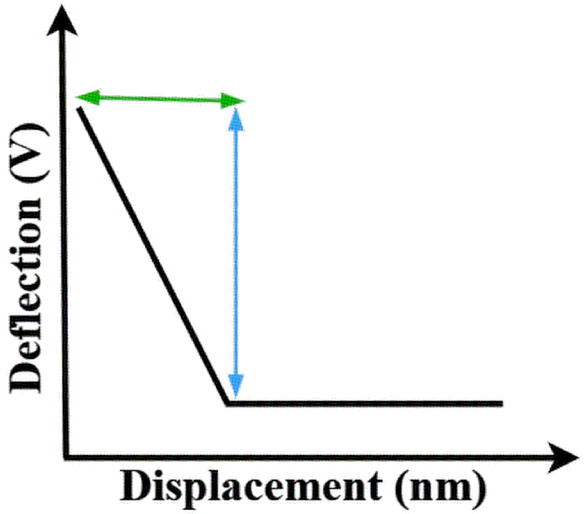

Source: Created by the author.

the slope of the contact region, being a necessary algorithm to obtain the characteristic spring constant of each cantilever. What we calculate manually is actually the *OLS*, given by:

$$OLS = \frac{cantilever\ deflection\ (V)}{LVDT\ displacement\ (nm)}. \tag{3.1}$$

Thus, InvOLS is exactly the reciprocal value of *OLS*.

After making the necessary corrections to the instrument, we managed to reach a precision that allows us to control essential factors for the feasibility of the measurements.

Therefore, following this protocol is essential to ensure, among other things, the alignment of the cantilever with the laser, in addition to predicting the depth of the cantilever indentation, thus indicating that the system is working properly.

3.2 Procedures

3.2.1 Measurement protocol

The experimental investigation was structured in two steps to comprehensively assess the mechanical properties of the material using AFM. In the initial experiment, we focused on the impact of the indentation speed controlled by the vertical scanning frequency f_z while keeping the applied force constant at 2 nN. Here, we vary the f_z frequency in a range of 0.25, 0.5, 1 and 2 Hz. An amplitude of the z piezo extension (ramp size) of 3 μm was adopted for all measurements. These scanning parameters result the vertical movement of the AFM tip with speeds of 1.5, 3.0, 6.0, 12 μ/s. In the next step, we varied the applied force, keeping the f_z frequency constant (at 0.5 Hz and 1.0 Hz). The applied forces were set to 1, 2, 4 and 8 nN, providing a variety of load conditions to study the material response. These experiments allowed us to consistently explore the influence of indentation speed and varying force regimes on the mechanical behavior of the cells.

3.2.2 Cell culture

In this research, we investigated two different cell lines individually—L929 and OF-COL II—which were duly adhered to the substrate and cultured following the protocol described in reference (SOUSA *et al.*, 2020). Both were cultured in high-glucose Dulbecco's modified Eagle's medium (DMEM) supplemented with 10% fetal bovine serum and 1% penicillin-streptomycin, and kept at 37°C in an atmosphere of 5% CO_2. Thus, to maintain stable pH outside the incubator, 2 ml of the medium was replaced with a PBS solution prior to AFM measurements. Besides, it is important to mention that all measurements were taken at room temperature, 25°C, within a maximum of two hours after removing the cells from the incubator.

3.2.2.1 L929 cells

Figure 17 shows the L929 cells analyzed in this work, which were derived from a mouse fibroblast cell line. Briefly, to understand the nomenclature of these cells, we need to analyze it in parts. First, the letter L refers to the name of the parent strain, which was derived from normal subcutaneous, areolar, and adipose tissue from a 100-day-old male C3H mouse (SANFORD *et al.*, 1948). Second, the number 929 refers to a subclone of strain L known as clone 929, obtained for the first time in 1948. These cells have significant relevance throughout the history of research and in diverse biomedical applications.

Figure 17 – Image of L929 fibroblast cells captured from the bottom camera of the AFM, during the initial stage of the experimental procedures. This demonstrates the confluence of the cell culture and its favorable conditions for measurements. It is also possible to observe the triangular microcantilever used in this work.

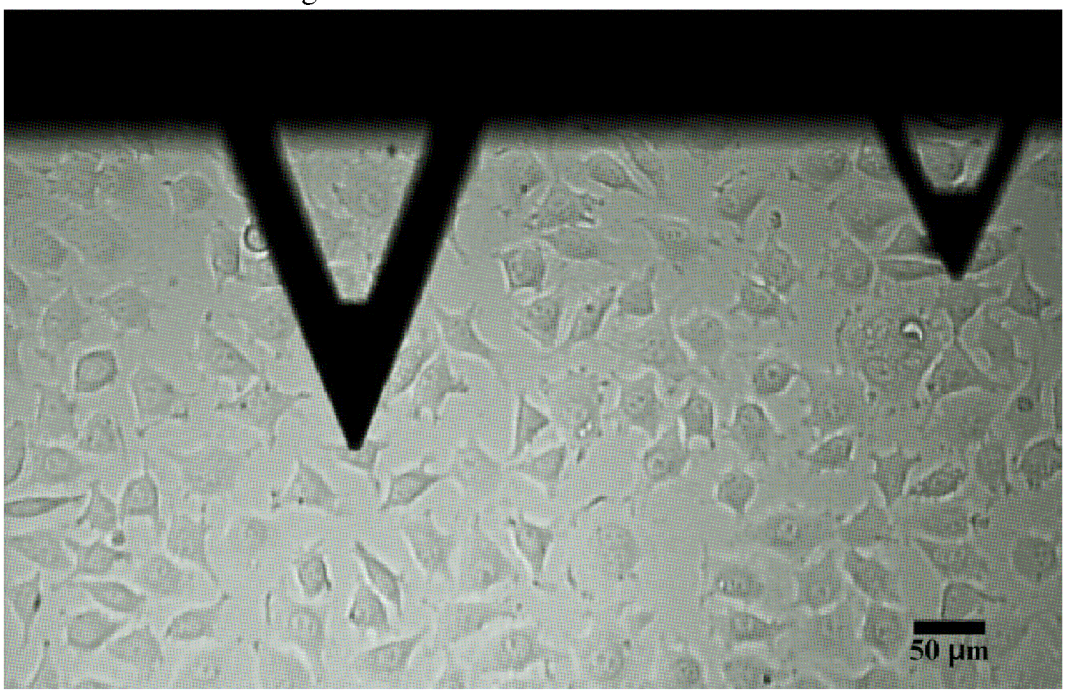

Source: Created by the author.

3.2.2.2 OFCOL II cells

The cell line OFCOL II originates from mice bone marrow (OLIVEIRA *et al.*, 2008). These cells are osteoblastic and typically reside on the bone surface, forming sheets of cubic or columnar structures. In addition, during our measurements, we used the AFM technique to capture a detailed image of the cell culture, as depicted in **Figure 18**. Interestingly, OFCOL II cells tend to be larger than L929 cells due to their specialized functions in the production of bone

matrix and the metabolic demands associated with this process.

Figure 18 – OFCOL II osteoblastic cells captured from the bottom camera of the AFM, during the initial stage of the experimental procedures. This demonstrates the confluence of the cell culture and its favorable conditions for measurements.

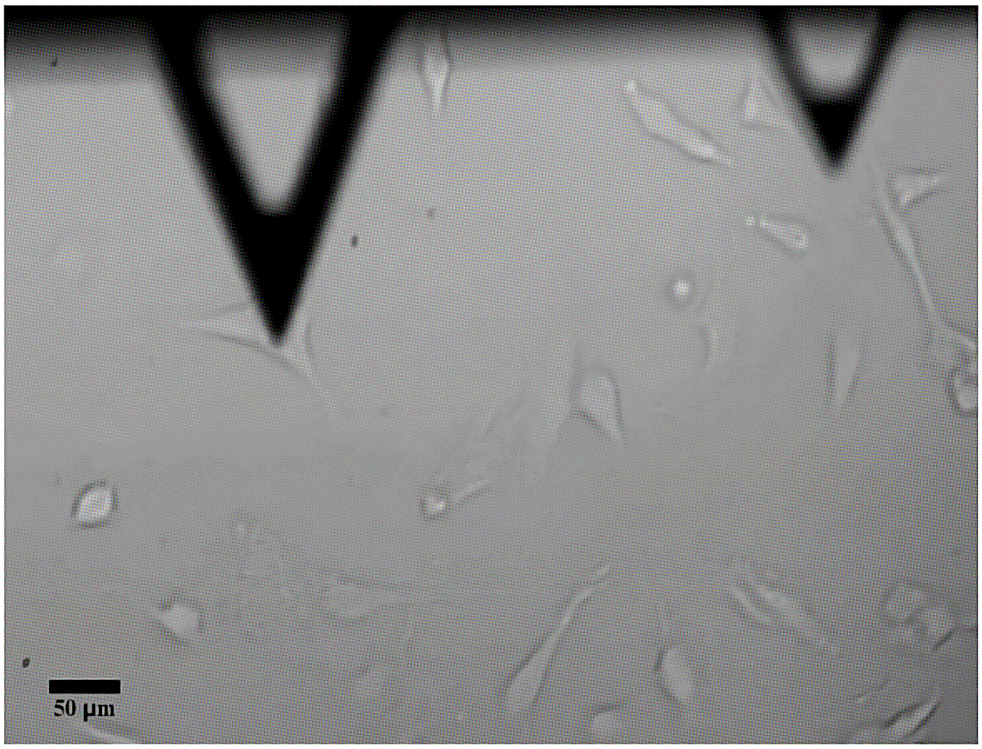

Source: Created by the author.

4 RESULTS AND DISCUSSIONS

4.1 AFM force measurements

AFM force curves exhibit the form $d = f(z)$, where d is cantilever deflection, and z is the corresponding translation of the piezoelectric actuator. A schematics of the indentation of a living cell by an AFM tip and a typical deflection-displacement curve measured in a cell are shown in **Figure 19**. The hysteresis in the approach/retract cycle is a consequence of the viscoelastic response of the sample. The maximum deflection (force) is controlled by a trigger algorithm to avoid excessive cell indentation. In this work, we used maximum forces varying between 1 nN and 8 nN. Beyond the contact point (z_0, d_0), the actual cantilever deflection is $\Delta d = d - d_0$, where d_0 is the cantilever deflection just before the contact with the sample surface. The corresponding piezo-actuator displacement is $\Delta z = z - z_0$, where z_0 represents the piezo displacement for which the cantilever touches the sample surface. The sample indentation δ is obtained with $\delta = \Delta z - \Delta d$. These quantities are graphically represented in **Figures 19a and b**.

Figure 19 – (a,b) Schematics of the indentation of a cell adhered by an AFM cantilever. $z(t)$ denotes the position of the triangular-shaped cantilever (in gray) relative to the sample surface, while $d(t)$ due to contact with the sample, and $\delta(t)$ represents the depth of indentation of the AFM tip in the sample. Graphic (c) Typical AFM force curve measured in a cell.

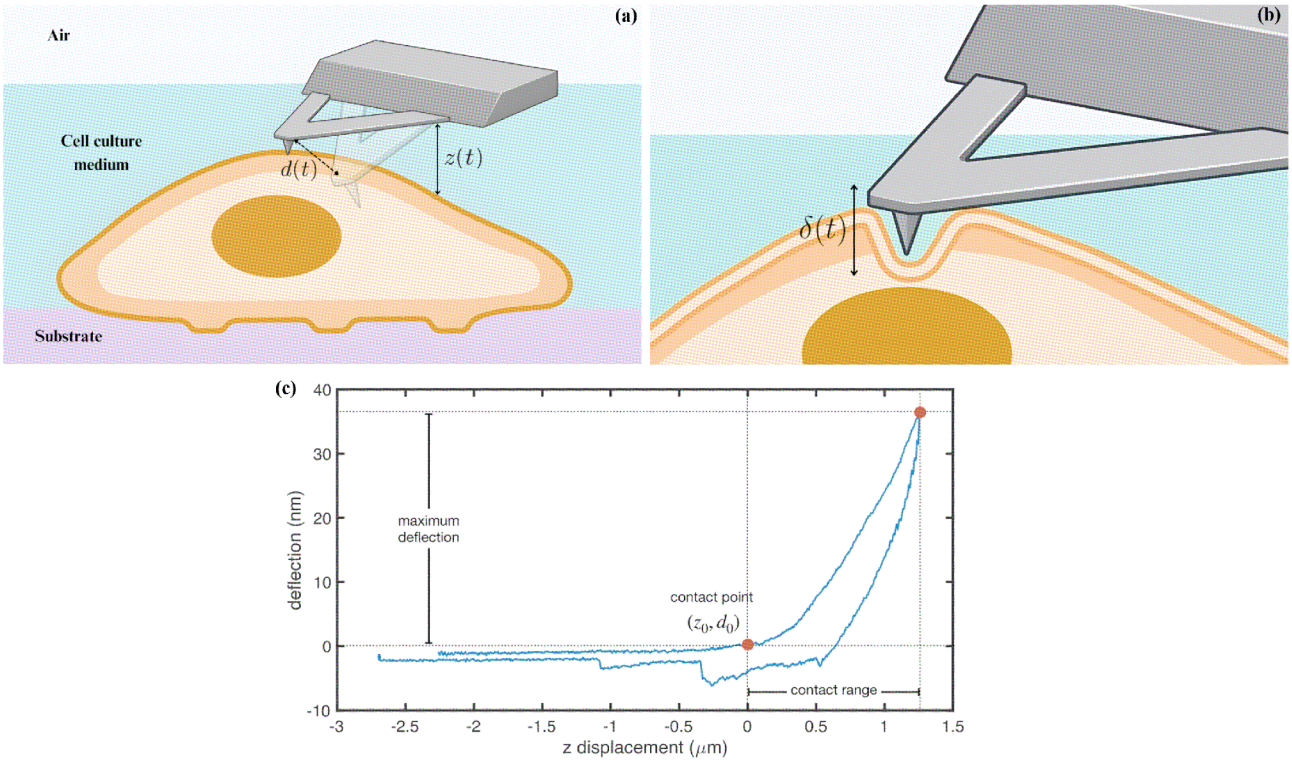

Source: Created by the author.

The force deflecting the cantilever is obtained by Hooke's law $F = k_c \Delta d$, where k_c is the cantilever spring constant. This force is transmitted to the sample causing an indentation. The relationship between cantilever deflection and sample indentation assume the general form $k_c \Delta d = F(\delta; E, \nu, \Omega(\lambda), h)$, where $F(\delta; E, \nu, \Omega(\lambda), h)$ is the force-indentation model that better represents the sample. (E, ν) represent the elasticity modulus and Poisson's ratio of the material, respectively. Samples are considered virtually incompressible ($\nu = 0.5$). Moreover, $\Omega(\lambda)$ represents a geometrical parameter of the indenter (e.g. the tip radius r for a spherical indenter or the half-opening angle θ for a conical indenter), and h represents the sample thickness. As illustrated in **Figure 20**, the chosen tip geometry significantly influences stress distribution, contact area and strain, resulting in specific mechanical responses. This underscores the importance of judiciously selecting indenter geometry to align with research objectives, ensuring an accurate interpretation of mechanical data and a comprehensive understanding of how cells respond to applied forces.

Figure 20 – Mechanical indentation of biological sample using varied geometric tips.

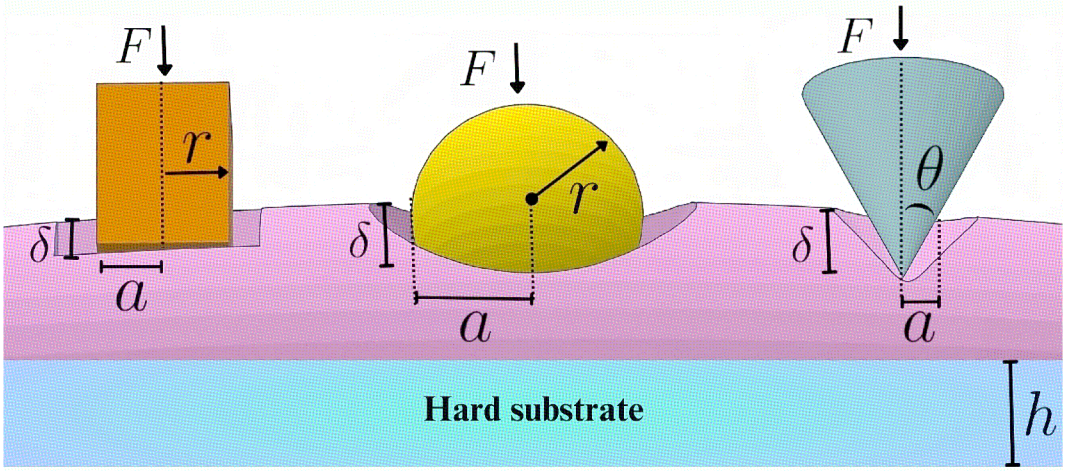

Source: Created by the author.

The analysis of force-indentation $F(\delta; E, \nu, \Omega(\lambda), h)$ curves are usually performed within the generalized Hertzian contact theory developed by Sneddon, that states that load-displacement relationships obey a power law $F \propto \delta^{\lambda}$, where the exponent λ and the proportionality factor depend on the indenter geometry (SNEDDON, 1965). Hertz theory is based on the following major assumptions: (i) the sample is assumed as a purely elastic half-space, (ii) the stress-strain response is linear, (iii) the *elasticity modulus is constant* (HERTZ, 1882). Therefore, Hertz model is not appropriate to describe viscoelastic materials. By taking into account all those assumptions, the final form of the Hertzian force-indentation model that will be used to

analyze the AFM forces curves takes the following form:

$$F_H(\delta) = \Omega(\lambda) E_H \delta^{\lambda}. \tag{4.1}$$

The subscript H stands for Hertz model, $\Omega(\lambda)$ and λ are geometry-dependent parameters, E is the elasticity modulus, and ν is the Poisson ratio ($\nu = 0.5$ for incompressible materials). The elasticity modulus E is related to the shear modulus G as $2G = E/(1+\nu)$. The parameters $\Omega(\lambda)$ and λ for different axisymmetric indenters are listed in Table 2. By writing the generalized Hertz model in terms of the measurable quantities provided by the AFM (z and d), one obtain the actual equation that is used to fit AFM force curves:

$$k_c(d - d_0) = \Omega(\lambda) E_H [(z - z_0) - (d - d_0)]^{\lambda} \tag{4.2}$$

for which there are three fitting parameters: E, z_0 and d_0.

Table 2 – Dependence of the parameters λ and $\Omega(\lambda)$ on the indenter geometry. Below, ν represents the Poisson ratio and δ is the indentation.

Geometry	λ	$\Omega(\lambda)$	contact radius	Obs.
flat cylinder	1.0	$\frac{2r}{(1-\nu^2)}$	r	r is the indenter radius
spherical	1.5	$\frac{4}{3}\frac{\sqrt{r}}{(1-\nu^2)}$	$\sqrt{r\delta}$	r is the indenter radius
conical	2.0	$\frac{2}{\pi}\frac{\tan\theta}{(1-\nu^2)}$	$\delta\tan\theta$	θ is the half-opening angle

Source: Created by the author.

It is noteworthy that knowing the geometry of each indenter and its respective applicability can be very useful during experimental measurements. While a spherical indenter establishes a circular contact region, a conical indenter generates an elliptical contact zone. Consequently, the deformation profile within the sample is directly influenced. In addition, spherical indenters induce localized deformations ideal for exploring microscale heterogeneities, whereas conical indenters offer a balance between localized and average measurements. On the other hand, flat cylindrical indenters enforce uniform deformation over the contact region, making them well-suited for studying planar mechanical cues, which typically involve forces or deformations that act parallel to a surface.

4.2 Viscoelastic response of cells

Cells are complex viscoelastic materials and their viscous response plays an important role during the indentation process. Darling *et al.* (DARLING *et al.*, 2007; DARLING *et*

al., 2006) and Ketene *et al.* (KETENE *et al.*, 2012) measured the viscous response of living cells, and suggested that those cells are well represented by the standard linear solid model (or Kelvin model) (FUNG, 1993). In this model, there are two elasticity moduli, one for the early instants of the indentation E_0, which Darling *et al.* called instantaneous elasticity modulus, and another elasticity modulus E_∞ for later instants of indentation. To obtain the apparent viscosity of samples with AFM, Darling *et al.* modified the closed-loop feedback control of the z-axis movement to perform stress relaxation tests in their samples (DARLING *et al.*, 2007; DARLING *et al.*, 2006).

The few references mentioned above are representative of very large body of experimental data that describes the viscoelastic properties of cells and tissues with simple viscoelastic models such as Maxwell, Kelvin-Voigt and the linear solid viscoelastic model (FUNG, 1993). These models, formed by association of springs and dashpots in series and parallel, are successful to describe the viscoelastic behavior exhibiting exponential relaxation decays with one (or few) characteristic timescale.

However, cells do not hold characteristic relaxation time. Instead, the complex architecture of living cells exhibits power-law (PL) relaxation. So far, the most used model to describe this cell mechanical behavior (even under pharmacological interventions) is the so called soft-glassy rheology (SGR) model (FABRY *et al.*, 2001; FABRY *et al.*, 2003). However, this model alone is neither able to describe other behavior commonly observed in cells (such as force generation, prestress and contractile stiffening) nor provide a microscopic origin of such behavior (KOLLMANNSBERGER; FABRY, 2011). There are a few studies proposing that cells exhibit a double PL shear modulus, $|G^*(\omega)| = A\omega^\alpha + B\omega^\beta$, with $\alpha > \beta$, where the higher and the lower exponents describe, respectively, the fast and slow dynamic response of the cell (DENG *et al.*, 2006; HOFFMAN *et al.*, 2006; HOFFMAN; CROCKER, 2009; REBELO *et al.*, 2014; RIGATO *et al.*, 2017). In this case, the storage modulus $G'(\omega)$ is well described by a single PL with low exponent of the order of $\beta = 0.2$ and the loss modulus $G''(\omega)$ described by two PL regimes, with a lower exponent identical to the exponent of $G'(\omega)$ and a fixed exponent $\alpha = 1$ for all samples. This *ad hoc* combination of PL responses is known as power-law structural damping model, and it was used as the theoretical basis to describe the dynamic rheology of cells in several works (FABRY *et al.*, 2001; FABRY *et al.*, 2003; MORALES *et al.*, 2001; ALCARAZ *et al.*, 2003; STAMENOVIĆ *et al.*, 2004; SMITH *et al.*, 2005). The fast relaxation regime is attributed to the entropic response of the individual F-actin filaments (DENG *et al.*, 2006). On

the other hand, the slow relaxation regime is attributed to the response of the cytoplasmic crowd, thereby related to the architecture and deformability of the whole cytoskeleton (FABRY *et al.*, 2001; FABRY *et al.*, 2003).

Since the fast relaxation only dominates in very small time scales (below few milliseconds), in this study we consider only the slow viscoelastic relaxation of cells, for which a single power-law relaxation function will be used. Such a function is written as:

$$E(t) = E_{ref}\left(\frac{t}{t_{ref}}\right)^{-\beta}, \tag{4.3}$$

where $E_{ref} = E(t_{ref})$ is a reference value of the elasticity modulus at an arbitrary scaling time, $t = t_{ref}$, and β is the relaxation exponent that lies in the range $0 \leq \beta \leq 1$. The elasticity modulus at any given time t can be obtained with the scaling rule $E(t)t^{\beta} = E(t_{ref})t_{ref}^{\beta}$. In this work, we assume $t_{ref} = 1$ s.

4.3 Power-law force model

The force-indentation relationship in time domain depends on the indentation depth history, $\delta(t)$, as well as on intrinsic properties of the sample and can be described by the following convolution integral (SOUSA *et al.*, 2020):

$$F(t) = \Omega(\lambda)\int_0^t E(t-t')\frac{d\delta^{\lambda}(t')}{dt'}dt', \tag{4.4}$$

where $E(t)$ is the time-dependent relaxation function of the material, and λ and $\Omega(\lambda)$ are parameters related to the indenter geometry (see Table 2). In order to obtain a realistic model, $\delta(t)$ must be as close to experimental conditions as possible. For this, we assume a linear indentation history during the loading/unloading phase of a regular force curve:

$$\delta(t) = \delta_0 \begin{cases} t/\tau_l & 0 \leq t \leq \tau_l, \\ 1/\tau_u[(\tau_l + \tau_u) - t] & \tau_l < t \leq \tau_l + \tau_u, \end{cases} \tag{4.5}$$

where τ_l is loading time, and τ_u is the unloading time.

For a regular AFM force curve (FC), the load (l) and unload (u) curves are, respectively, obtained by solving the following integrals:

$$F_l(t) = \Omega(\lambda)\int_0^t E(t-t')\frac{d\delta_l^{\lambda}(t')}{dt'}dt' \quad (t \leq \tau_l), \tag{4.6}$$

$$F_u(t) = \Omega(\lambda)\int_0^{\tau_l} E(t-t')\frac{d\delta_l^{\lambda}(t')}{dt'}dt' + \int_{\tau_l}^t E(t-t')\frac{d\delta_u^{\lambda}(t')}{dt'}dt' \quad (t \geq \tau_l). \tag{4.7}$$

The solution of those integrals for PL materials yields:

$$F_l(t) = \lambda\Omega(\lambda)B(\lambda, 1-\beta)E_\beta(\tau_l)\delta_0^\lambda \left(\frac{t}{t_l}\right)^{\lambda-\beta}. \tag{4.8}$$

$$F_u(t) = \lambda\Omega(\lambda)B(\tau_l/t, \lambda, 1-\beta)E_\beta(\tau_l)\delta_0^\lambda \left(\frac{t}{t_l}\right)^{\lambda-\beta} + \ldots$$
$$\ldots - \lambda\Omega(\lambda)E_\beta(\tau_l)\delta_0^\lambda \frac{\tau_l^\beta}{\tau_u^\beta}\frac{1}{1+\beta}\left(\frac{t-\tau_l}{\tau_u}\right)^{1-\beta} {}_2F_1\left(1, 1-\lambda, 2+\beta; \frac{t-\tau_l}{\tau_u}\right). \tag{4.9}$$

${}_2F_1(a,b,c;x)$ is the Gauss hypergeometric function. In the force model above, we determined both loading and unloading curves just for the sake of completeness. As the whole viscoelastic relaxation properties are embedded in the loading curve alone, we will focus our analysis in the loading portion because of its mathematical simplicity. Equation 4.8 can be written in different forms, revealing alternative ways to interpret it:

Method 1: In the time domain, Equation can be written as

$$F_l(t) = F_0 \left(\frac{t}{t_l}\right)^{\lambda-\beta}, \tag{4.10}$$

$$F_0 = \lambda\Omega(\lambda)B(\lambda, 1-\beta)E_\beta(\tau_l)\delta_0^\lambda \tag{4.11}$$

where F_0 is the maximum cantilever force in the end of the loading curve, which can be controlled by imposing a trigger force in the measurements. Such a form, shows that F_0 depends on the indenter geometry, maximum indentation depth and speed, and on the material properties. One should note that this equation can also be written in the indentation domain as $F_l(\delta) = F_0(\delta/\delta_0)^{\lambda-\beta}$. In a log-log plot, loading force curve obeys a power-law whose exponent directly shows the viscoelastic relaxation exponent.

Method 2: In the indentation domain, Equation 4.8 can be written in a Sneddon's-like form with a time-dependent Young's modulus $E_H(t)$.

$$F_l[\delta(t)] = \Omega(\lambda)E_H(t)\delta^\lambda(t), \tag{4.12}$$

$$E_H(t) = \lambda B(\lambda, 1-\beta)E(t). \tag{4.13}$$

In the case of $\beta = 0$ the above equation recovers the the Sneddon's model for perfectly elastic materials, i.e., $E(t)$ is time-independent. Equation 4.12 reveals an important detail, which is

normally overlooked when using Sneddon's model to study viscoelastic materials. The Young modulus will depend on the duration of the loading curve if the whole curve is fitted, or the time range of the curve portion used in the fitting processes. Moreover, the Young's modulus not only will depend on the type of indenter, but it will be larger than the actual elasticity modulus by a factor of $E_H(t)/E(t) = \lambda B(\lambda, 1-\beta)$. Since living cells are well represented by $\beta \approx 0.2$, this measured Young's modulus must be corrected by 1.39, 1.33 and 1.25 for conical, spherical and flat indenter geometries, respectively. The Young's modulus measured with conical tip must be 4.5% and 11% larger than the ones measured with spherical and flat indenters for the same duration of the loading curve, while the Young's modulus measured with spherical indenters must be larger 6.5% than the ones measured with flat ones. Finally, due to the explicit time-dependence of $E_H(t)$ in Equation 4.12, the approximate relaxation function of a power-law material can be directly obtained in a single loading force curve by making:

$$E(t) \propto \frac{F(t)}{\lambda \Omega(\lambda) \delta^{\lambda}(t)}. \tag{4.14}$$

4.4 Simulation of AFM force curves in power-law materials

Force curves measured in materials exhibiting power-law relaxation function can be simulated by assuming the time-dependence of the parameters $d(t)$, $z(t)$ and $E_H(t)$ in Equation 4.2, which becomes:

$$k_c(d(t) - d_0) = \Omega_\lambda E_H(t)[(z(t) - z_0) - (d(t) - d_0)]^{\lambda}. \tag{4.15}$$

where the piezo displacement extends linearly $z(t) = z_i \pm v_z t$, where z_i is the initial piezo position, and the signal $\pm$ indicates whether the piezo is approaching to or moving away from the sample surface. Equation 4.15 for $d(t)$ for each t, one can simulate approach and retract AFM force curves for power-law materials.

Figures 21a and **b** show simulated AFM force curves measured with different piezo extension rates f_z and indenter geometries, subjected to a maximum trigger force of 2 nN. The curves F versus z clearly shows that both f_z and tip geometry will have a strong effects in the perceived Young modulus of the samples. Fixing f_z, measurements made with a conical indenter yields the smallest Young´s modulus, while measurements made with a flat cylinder the largest. This is in general justified in terms of contact area, which is smallest for the conical shape, and largest for the flat cylinder. Thus, for a fixed force, the largest is the contact area, the smaller becomes the indentation depth, thereby yielding larger Young´s modulus. This simple analysis

is accurate for perfectly elastic samples. However, soft materials are intrinsically viscoelastic and time becomes a very important variable. **Figure 21b** shows that duration of the force curves varies drastically not of for different f_z, but also for different indenter geometries. Thus, when probing viscoelastic materials with the AFM, even if ther standardize the maximum applied forces, we are in fact probing not only different indentation depths, but also different times.

By changing f_z, while keeping the maximum force fixed at 2 nN, we obtain loading times ranging within nearly three orders of magnitude (few ms to few seconds). Such a range is wide enough to reveal the relaxation properties of many types of soft samples. In fact, plotting the fitted Young's moduli values versus the approach times of the force curves in each frequency, we obtain a function that differs from the actual relaxation function by a fixed factor such that $E_H(t) = \lambda B(\lambda, 1-\beta)E(t)$, as shown in **Figure 22b**. Such a behavior is very robust and independent on the type indenter geometry. Finally, despite of the assumption of Sneddon's model to be valid only for purely elastic materials, by probing samples with wide enough range of f_z frequencies, we can reconstruct the underlying relaxation function of the samples.

Although the simulated force curves have confirmed that the fitted Young moduli differ from the actual relaxation function a fixed factor $E_H(t)/E(t) = \lambda B(\lambda, 1-\beta)$, this needs to be validated in living cells which, despite having been widely demonstrated to relax according to a power-law, its properties are highly inhomogeneous over the cell surface.

One should note that the relaxation exponent determined from the fitting of $E_H(t_l)$ versus $E(t_l)$ is identical to the exponent determined from the fitting $E_H(t_l)$ alone measured for various f_z frequencies. Therefore, it is clear that the fitting of the force curves with generalized Hertz (Sneddon's) model alone is enough to determine the viscoelastic relaxation of the cells.

4.5 Application of the model with L929 cells

Figure 22 shows force curves measured at the same spot of a L929 mouse fibroblast with different f_z frequencies, subjected to 2 nN of maximum force. Increasing the frequency reduces the loading time t_l and maximum indentation depth, and induces an increase in the measured Young's modulus. In this way, such behavior is predicted by Eq. 4.11 that shows that the Young's modulus is inversely proportional to the indentation depth for a fixed F_0. In fact, since F_0, δ_0 and t_l can be directly obtained from the force curves, Eq. 4.11 can be used to quickly estimate of $E(t_l)$.

However, living cells are highly inhomogeneous, and we measure 16 force curves

Figure 21 – Simulated AFM foce curves of a power-law material ($E_{ref} = 1$ kPa, $t_{ref} = 1$ s, $\beta = 0.2$) measured with different f_z frequencies and indenter geometries. The parameters used to generate these curve as $k_c = 0.06$ N/m, R = 2.5 μm (flat cylinder and spherical indenters), $\theta = 38^o$ (conical indenter). All force curves are subjected to maximum trigger force of 2 nN. (c) Relationship between the approach time of simulated force curves as a function f_z. All simulated curves were generated using identical parameters, except for f_z. (d) Comparison of the fitted (solid symbols) and corrected (open symbols) Young´s moduli with the actual underlying power-law relaxation curve.

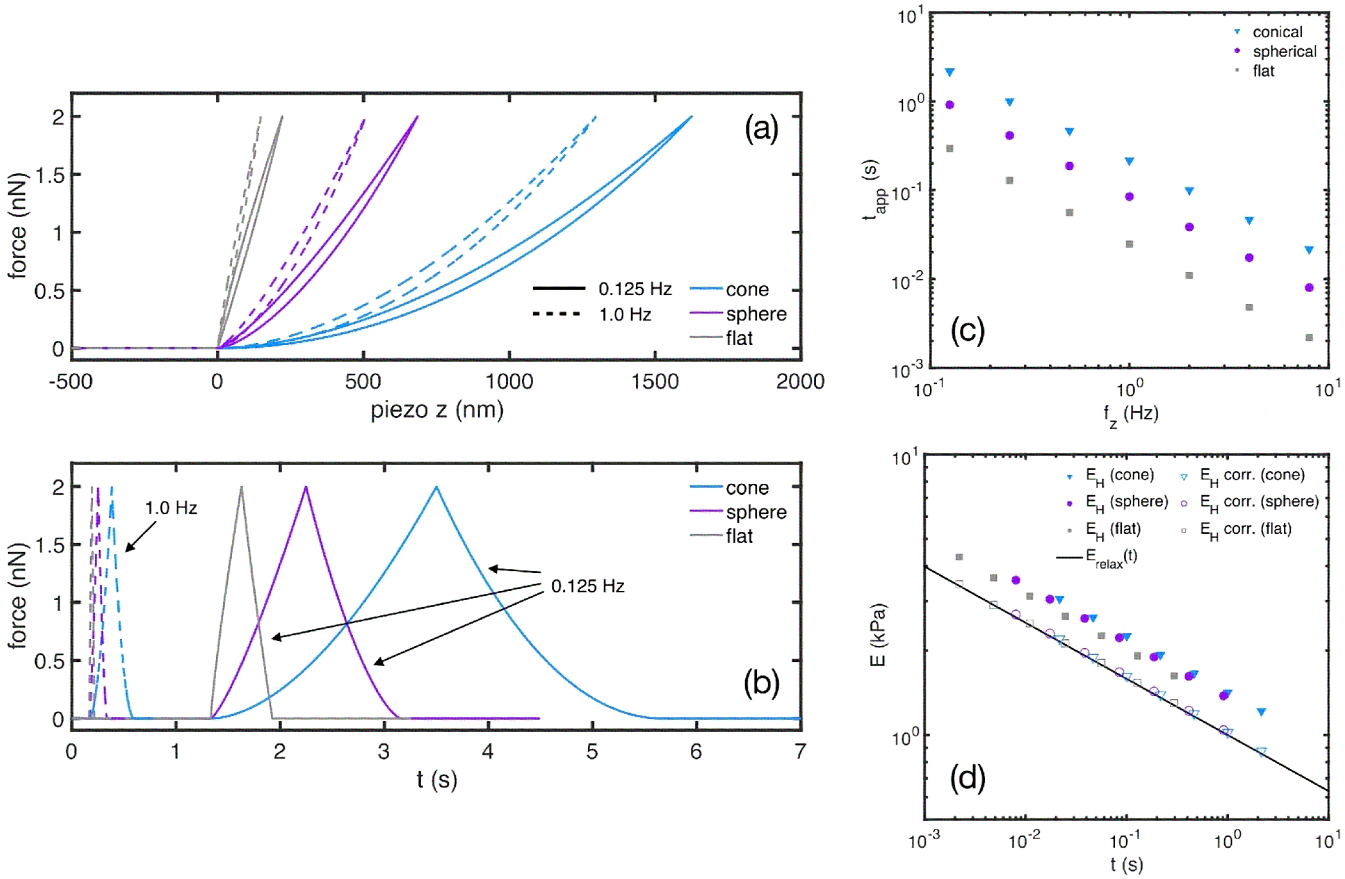

Source: Created by the author.

over a squared area of $4\mu m$ of side of a single cell with several f_z frequencies. Each curve is fitted with Equations 4.11 and 4.12 to obtain $E(t_l)$ and $E_H(t_l)$ respectively, and the relationship of those elasticity moduli are shown in **Figure 23a**.

The data points clearly shows a direct scaling between $E(t_l)$ and $E_H(t_l)$. By fitting the data points with Eq. 4.13 we obtain an average relaxation exponent of $\beta = 0.13$, which can be regarded as an average relaxation exponent to describe the whole cell as an homogeneous viscoelastic body. One should note that Equation 4.13 does not involve time, which is only implicitly considered by including data points measured for different values of f_z. Time can be explicitly considered by plotting $E_H(t_l)$ versus t_l, shown **Figure 23b** (colored data points). In time domain, the data span across one order of magnitude (from 0.05 s to 2 s). Here, the position-

Figure 22 – Samples of AFM force curves measured with different f_z in the same spot of the surface of a L929 mouse fibroblast. The inset graph shows the force curves in time domain. The dashed lines represent the fitting of the loading curves with Hertz´s model. The curves are horizontally aligned by contact point, and shifted vertically for better visualization.

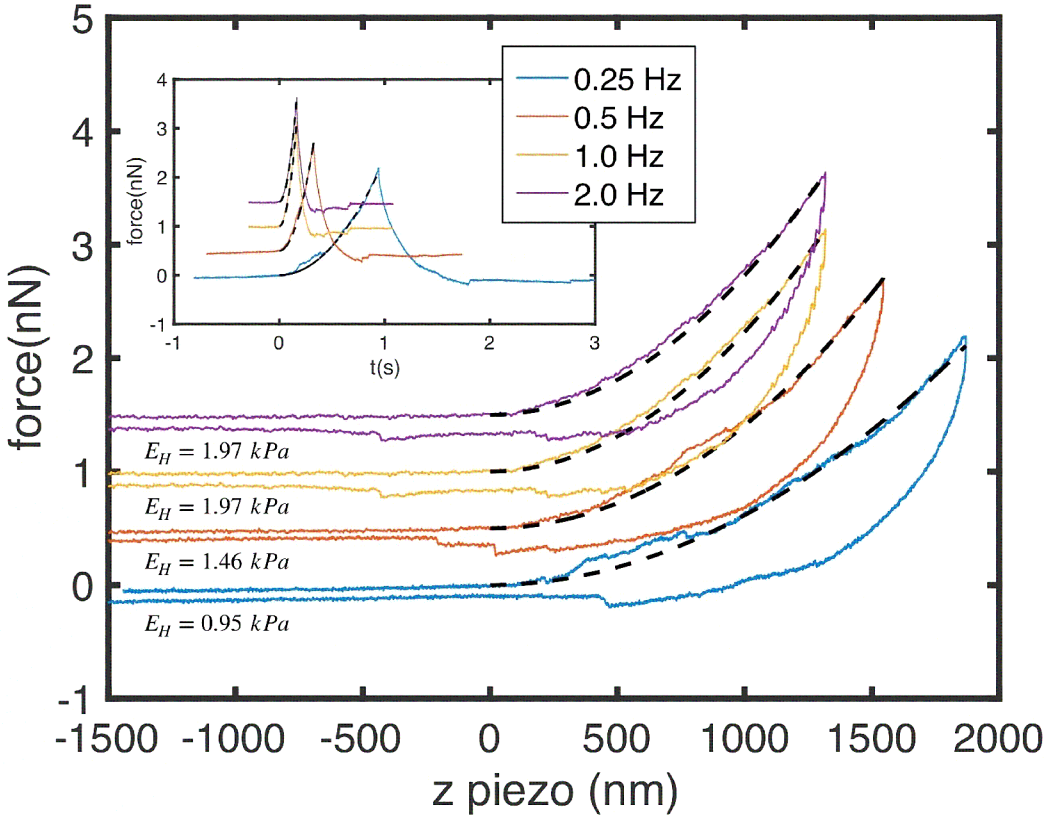

Source: Created by the author.

dependent dispersion of $E_H(t_l)$ becomes evident, exhibiting a dispersion width of 1 kPa. In order to obtain the viscoelastic relaxation function, we first determine the median values of $E_H(t_l)$ per f_z (black squares). Since this data exhibit the same power-law time-dependence of $E(t)$, the average values of $E_H(t_l)$ are fitted with a single power-law relaxation function $At^{-\beta}$ to obtain an average relaxation exponent $\beta = 0.14$. This value is then used to calculate the correction factor $\lambda B(\lambda, 1-\beta)$ and use Eq. 4.13 to determine the actual $E(t_l)$ (red squares), whose fitting with a power-law relaxation function provides and elasticity modulus $E(1) = 1.016$ kPa. According to Equation 4.3, the parameters $E(1)$ and β fully determine the average viscoelastic relaxation of the measure cell.

4.5.1 Determination of $E(t)$ from a single force curve

Equation 4.13 shows that fitting a force curve $F(t)$ versus $\delta(t)$ using generalized Hertz's model provides $E_H(t)$, where t is time duration that the tip takes to achieve and indentation

Figure 23 – Analysis of elasticity moduli and viscoelastic relaxation in the experimental data of L929 cells. (a) Elasticity moduli relationship and direct scaling. (b) Time-dependent dispersion of $E_H(t_l)$ and viscoelastic relaxation. (c) Median values of $E_H(t_l)$ per f_z (black squares) for viscoelastic relaxation function.

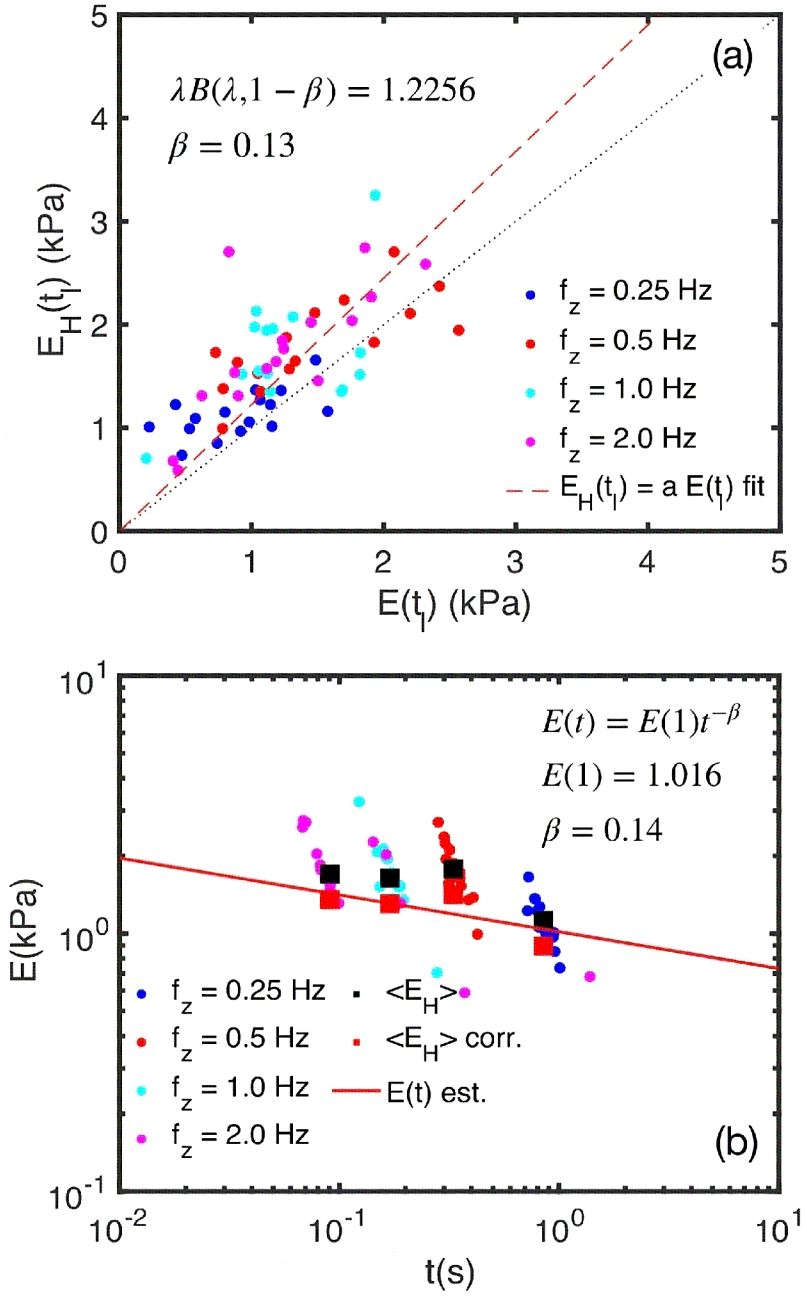

Source: Created by the author.

depth of $\delta(t)$. This makes us wonder whether we can take advantage of force curves measured with low f_z frequency and progressively fit $F(t)$ versus $\delta(t)$ with a sliding time width up to $t = t_l$. Moreover, in this work, the force curves were measured with sampling rate of 2 kHz, which represents a resolution in time of $\Delta t = 0.5$ ms. By splitting the forces curves is slots of 30 Δt, one can fit a single force curve in up to $n \times (15\ ms)$, where $n = 1, 2, ..., N$ $(N \times (15\ \Delta t)) = t_l$.

Figure 24 – (a) Approach portion of the force curves of **Figure 22** in time domain. (b) Log-log plot of the force curves. The vertical bars indicate the end points of each fitting window of the Hertz model. (c) Comparison of the time-dependent Young´s moduli $E_H(t)$ determined using Equation 4.13 (solid lines) and Hertz model (dashed lines).

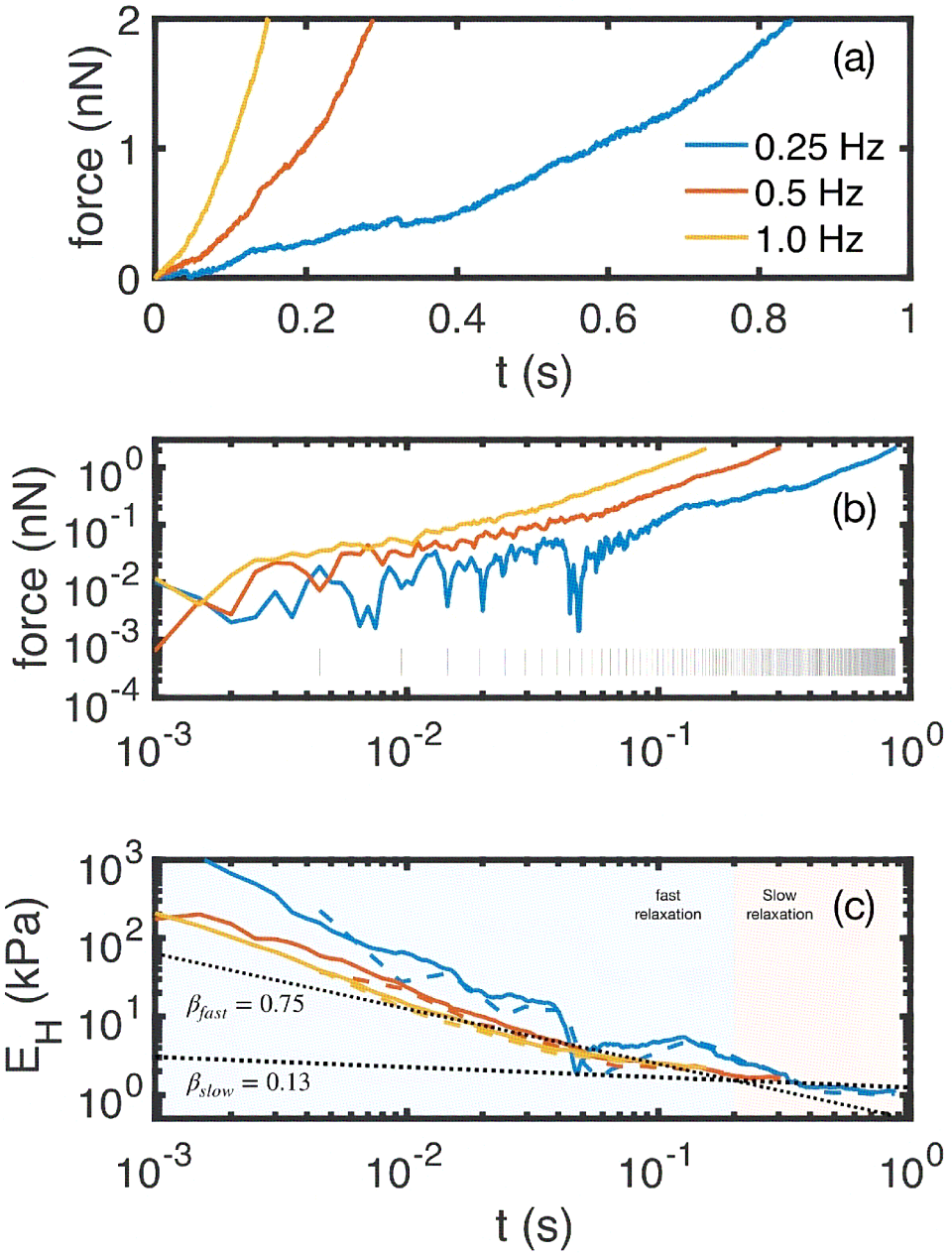

Source: Created by the author.

To demonstrate this analysis, we depart from the force curves shown in **Figure 22**, which are shown in **Figure 24a** in time domain, from the contact point up to the maximum force. These curves are also shown in log-log plot in **Figure 24b**, where the vertical line show the end points of each fitting window where the Hertz's analyses are performed. **Figure 24c** shows the time dependence of $E_H(t)$ constructed with two methods: (i) using Eq. 4.13 (solid lines), and

(ii) by fitting the force curves with Hertz's model using the sliding time window (dashed lines). The agreement between both methods is undeniable. Moreover, the $E_H(t)$ curves for different f_z are very similar exhibiting two relaxation regimes, a fast relaxation regime (up to 200 ms) with exponent $\beta_{fast} = 0.75$, and a slow relaxation regime for larger observation times with exponent $\beta_{fast} = 0.13$, nearly identical to the exponent obtained by analysing the entire range of multiple force curves measured with different f_z's (shown in **Figure 23**). This fast relaxation regime has been observed in many reports in time and frequency domains (DENG *et al.*, 2006; RIGATO *et al.*, 2017; SOUSA *et al.*, 2020).

Two important points are worth to mention. First, we remind that the actual relaxation function $E(t)$ can be obtained from $E_H(t)$ using Equation 4.13. The only missing factor is the slow relaxation exponent β, which can be extracted by fitting $E_H(t)$ with a single power-law function $At^{-\beta}$ for larger timescales ($t > 100$ ms). Second, each $F(t)$ curve shown in **Figure 24** is representative of a single point in the cell surface. In order to estimate an average $\langle E(t) \rangle$ for the whole cell, it is necessary to determine $E(t)$ over several points in the cell surface and compute an average function.

4.6 Robustness of the model

The most important result of this work is the model of Equation 4.13 that shows how the Young's modulus of the generalized Hertz model E_H is related to the time-dependent elasticity modulus $E(t)$ of material described by a single power-law viscoelastic relaxation. So far, this model was tested with measurements made in a single L929 cell. In order to demonstrate the robustness of the model, it is important to test it with a large volume of data.

The same experimental protocol used in **Figure 23**, i.e., measuring 16 forces curves per cell with different vertical frequencies and maximum force of 2 nN, in two different cell lines for $n_{L929} = 13$ and $n_{OFCOLII} = 16$ cells. Each force curve is fitted with Hertz model (Equation 4.12) to determine E_H using the whole extent of the force. The curves are also fitted the single PL model (Equation 4.8) to extract both $E(t_l)$ and β. With these quantities, the estimated Young modulus $E'_H = \lambda B(\lambda, 1-\beta)E(t_l)$ is calculated and compared to the actual E_H. The results are shown in **Figure 25**.

The histograms clearly show that the measured E_H are consistently larger than $E(t_l)$ despite of the frequency fz and type of cell, which in qualitative agreement with Equation 4.13. The data also show that OFCOL II cells are slightly stiffer than L929 ones. OFCOL II cells

Figure 25 – Distribution of measured values of E_H (a,e), $E(t_l)$ (b,f), relaxation exponent β (c,g) and difference $E_H - E'_H$ (d,h), where $E'_H = \lambda B(\lambda, 1-\beta)E(t_l)$ is the Young's moduli estimated from the time-dependent relaxation model (Equation 4.13). All force curves are subjected to a maximum force of 2 nN. The number of measured cells per cell line is $n_{L929} = 13$ and $n_{OFCOLII} = 16$ cells. In each

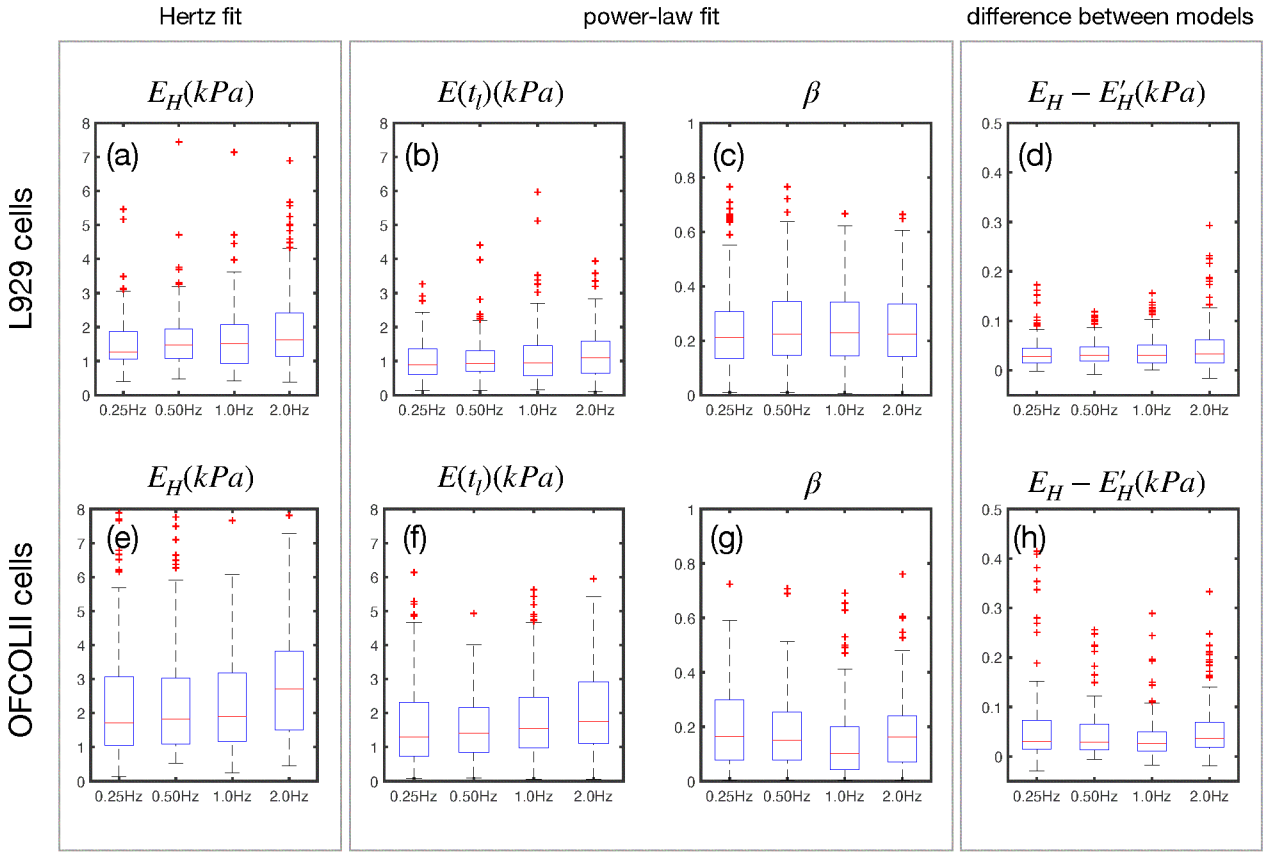

Source: Created by the author.

also exhibit an slightly larger solid-like character (lower values of the viscoelastic exponent β) compared to L929 cells. These characteristic hold for all vertical frequencies. The vertical frequency has little influence in the average elasticity moduli and relaxation exponent. The histograms of E'_H are not explicitly shown but the distribution of the error $\Delta E_H = E_H - E'_H$ shows that both models agree quite well, exhibiting an average difference of approximately 0.03 kPa for curves measured with frequencies up to $f_z = 2Hz$.

To confirm the robustness of the model for maximum forces above 2 nN, we also performed the same measurements by fixing the vertical frequency at $f_z = 0.5$ Hz and varied the maximum forces from 1 nN up to 8 nN. The results are shown in **Figure 26**.

The elastic moduli E_H and $E(t_l)$ increase with an increase in the maximum force. This stress stiffening is a well known nonlinear mechanical response of the living cells (KOLLMANNSBERGER *et al.*, 2011). The ratio $\langle E_H \rangle_{8nN} / \langle E_H \rangle_{1nN}$ shows that the nonlinear stiffening

Figure 26 – Distribution of measured values of E_H (a,e), $E(t_l)$ (b,f), relaxation exponent β (c,g) and difference $E_H - E'_H$ (d,h), where $E'_H = \lambda B(\lambda, 1-\beta)E(t_l)$ is the Young's modulus estimated from the time-dependent relaxation model (Equation 4.13). All force curves are subjected to $f_z = 0.5$ Hz. The number of measured cells per cell line is n = 15 and n = 16 cells. In each

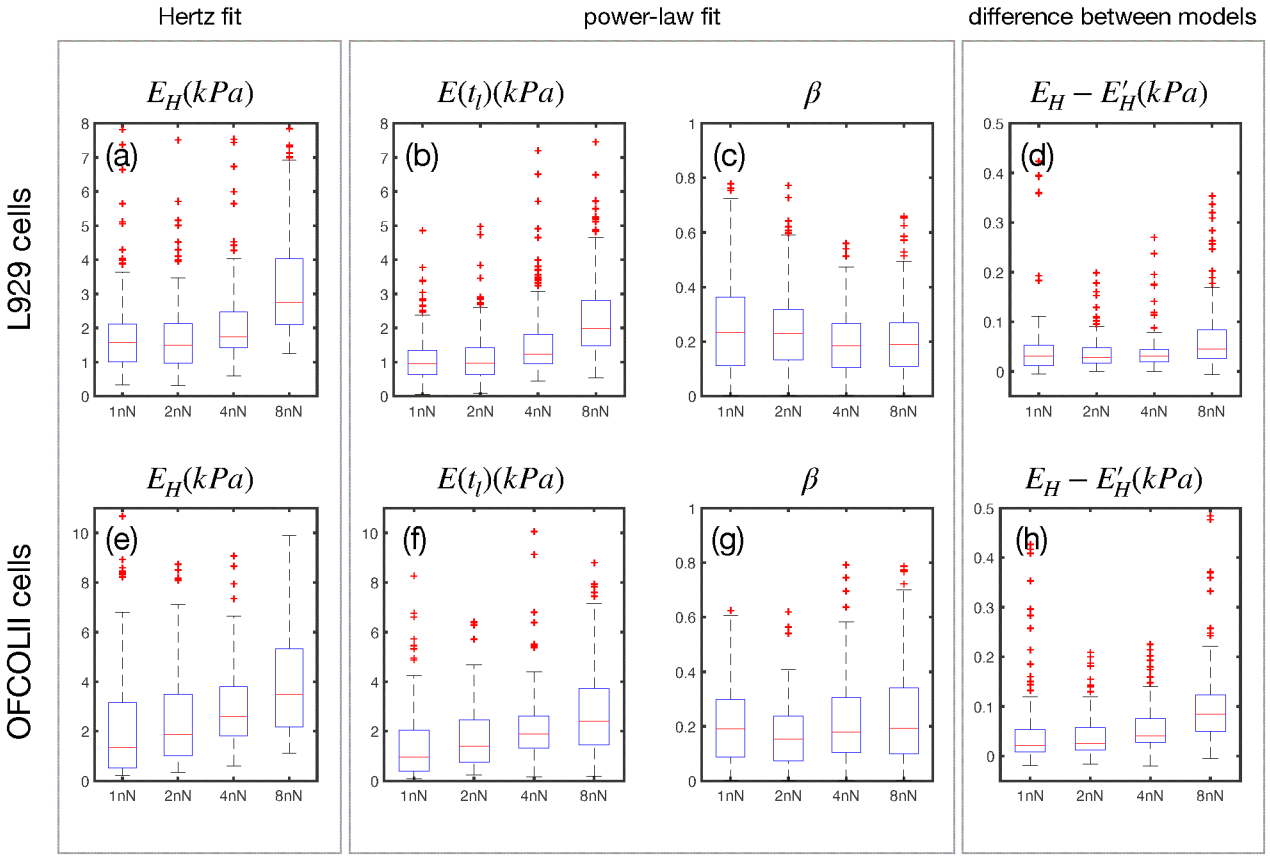

Source: Created by the author.

is larger in OFCOL II cells than in L929 ones. On the other hand, the relaxation exponent of the OFCOL II cells seems independent of the maximum force, while L929 cells exhibit an slight enhancement of its solid-like response (lower exponents) for increasing forces. This seems to be in contradiction with the work of Kollmannsberger *et al.* (2011) who shown that the relaxation exponent increases with increasing external stresses (KOLLMANNSBERGER *et al.*, 2011).

Finally, the analysis of $\Delta E_H = E_H - E'_H$ shows that the difference between models exhibit differences of the order of few tens Pa, but this error increases as the applied forces increases, and the error seems cell-dependent being larger for OFCOL II cells than for L929 ones. Anyhow, we can conclude that the model of Equation 4.13 is robust enough to account for nonlinear mechanical deformation of living cells.

5 CONCLUSIONS AND FUTURE WORK

The main scientific objetive of this master's thesis is to demonstrate the relationship between the generalized Hertz model, derived to describe the deformation properties of semi-infinite elastic materials by axisymmetric indenters, and the time-dependent viscoelastic relaxation properties of living cells.

Hertz model is largely used to study the mechanical response of cells and tissues under different pharmacological and pathological conditions. Despite of the fundamental assumptions that, in principle, prevent the use of Hertz model to study viscoelastic materials, the model developed in this work shows that it is possible to quantitatively determine the underlying viscoelastic relaxation function of the cells.

The most important result of this thesis is the model of Eq. 4.13 that shows how the relationship of the Young's modulus E_H obtained from the generalized Hertz model with the time-dependent elasticity modulus $E(t)$ measured at the instant where the AFM cantilever achieves the maximum force. This expression assumes that living cells are described by a single power-law viscoelastic relaxation (see Eq. 4.3).

The validity and robustness of the model was tested by measuring tens of living cells from two different lines (L929 and OFCOLII) under different loading conditions, namely (i) fixed force and varying indentation velocities (varying f_z), and (ii) fixed f_z and varying forces. In both cases, the difference between the fitted E_H and the estimated Young's modulus E'_H derived from the viscoelastic force model (Eq. 4.8) is very small compared with the actual stiffness of the cells (of the order of few tens of Pa). The model is valid even in the regime of nonlinear stress stiffening (higher applied forces).

In conclusion, the present study has significant experimental and theoretical implications, contributing to a more comprehensive understanding of both linear and nonlinear mechanical properties of cells within the framework of the Generalized Hertz model. Our model open up new avenues for future research in nonlinear cell mechanics and provide a simplified theoretical framework for further investigations in cellular behaviors under complex mechanical environments.

REFERENCES

ABERCROMBIE, M.; HEAYSMAN, J. E.; PEGRUM, S. M. The locomotion of fibroblasts in culture: Iv. electron microscopy of the leading lamella. **Experimental Cell Research**, Elsevier, v. 67, n. 2, p. 359–367, 1971.

ALCARAZ, J.; BUSCEMI, L.; GRABULOSA, M.; TREPAT, X.; FABRY, B.; FARRÉ, R.; NAVAJAS, D. Microrheology of human lung epithelial cells measured by atomic force microscopy. **Biophysical Journal**, v. 84, n. 3, p. 2071–2079, 2003.

AMBLARD, F.; YURKE, B.; PARGELLIS, A.; LEIBLER, S. A magnetic manipulator for studying local rheology and micromechanical properties of biological systems. **Review of Scientific Instruments**, AIP Publishing, v. 67, n. 3, p. 818–827, 1996.

ASHEGHI, M.; BENDER, J. W.; DEVASENATHIPATHY, S.; GARDEL, M. L.; KRIM, J.; MEINHART, C. D.; RUOFF, R. S.; SANTIAGO, J. G.; VALENTINE, M. T.; WEITZ, D. A.; WERELEY, S. T.; YANG, Y.; YU, M.-F. **Microscale Diagnostic Techniques**. [S.l.]: Springer Berlin, Heidelberg, 2005. ISBN 978-3-540-26449-1.

ASHKIN, A.; DZIEDZIC, J. M.; BJORKHOLM, J. E.; CHU, S. Observation of a single-beam gradient force optical trap for dielectric particles. **Optics Letters**, v. 11, n. 5, p. 288–290, 1986.

BARNES, H. A. **A Handbook of Elementary Rheology**. [S.l.]: The University of Wales Institute of Non-Newtonian Fluid Mechanics, 2000. ISBN 0-9538032-0-1.

BARNES, H. A.; HUTTON, J. F.; WALTERS, K. **An Introduction to Rheology**. [S.l.]: Elsevier, 1989. ISBN 0-444-87140-3.

BINGHAM, E. C. The nature of fluid flow. **Journal of Chemical Education**, v. 6, n. 6, p. 1113–1119, 1929.

BINNIG, G.; QUATE, C.; GERBER, C. Atomic force microscope. **Physical Review Letters**, v. 56, n. 9, p. 930–934, 1986.

BURRIDGE, K.; FATH, K.; KELLY, T.; NUCKOLLS, G.; TURNER, C. Focal adhesions: transmembrane junctions between the extracellular matrix and the cytoskeleton. **Annual Review of Cell Biology**, v. 4, n. 1, p. 487–525, 1988.

CICUTA, P.; DONALD, A. M. Microrheology: a review of the method and applications. **Soft Matter**, v. 3, n. 12, p. 1449–1455, 2007.

CLARK, M. A.; CHOI, J.; DOUGLAS, M. **Biology 2E**. [S.l.]: OpenStax: Rice University, 2018. ISBN 978-1-947172-52-4.

DARLING, E.; ZAUSCHER, S.; GUILAK, F. Viscoelastic properties of zonal articular chondrocytes measured by atomic force microscopy. **Osteoarthritis and Cartilage**, Elsevier, v. 14, n. 6, p. 571–579, 2006. Available at: https://doi.org/10.1016/j.joca.2005.12.003.

DARLING, E. M.; ZAUSCHER, S.; BLOCK, J. A.; GUILAK, F. A thin-layer model for viscoelastic, stress-relaxation testing of cells using atomic force microscopy: Do cell properties reflect metastatic potential? **Biophysical Journal**, Elsevier, v. 92, n. 5, p. 1784–1791, 2007. Available at: https://doi.org/10.1529/biophysj.106.083097.

DEJANA, E. Endothelial cell–cell junctions: happy together. **Nature Reviews Molecular Cell Biology**, v. 5, n. 4, p. 261–270, 2004.

DENG, L.; TREPAT, X.; BUTLER, J. P.; MILLET, E.; MORGAN, K. G.; WEITZ, D. A.; FREDBERG, J. J. Fast and slow dynamics of the cytoskeleton. **Nature Materials**, v. 5, n. 8, p. 636–640, 2006.

FABRY, B.; MAKSYM, G. N.; BUTLER, J. P.; GLOGAUER, M.; NAVAJAS, D.; FREDBERG, J. J. Scaling the microrheology of living cells. **Physical Review Letters**, v. 87, n. 14, p. 148102, 2001. Available at: http://hdl.handle.net/2445/12785.

FABRY, B.; MAKSYM, G. N.; BUTLER, J. P.; GLOGAUER, M.; NAVAJAS, D.; TABACK, N. A.; MILLET, E. J.; FREDBERG, J. J. Time scale and other invariants of integrative mechanical behavior in living cells. **Physical Review E**, v. 68, n. 4, p. 041914, 2003.

FLORMANN, D.; ANTON, C.; POHLAND, M.; BAUTZ, Y.; KAUB, K.; TERRIAC, E.; SCHÄFFER, T.; RHEINLAENDER, J.; JANSHOFF, A.; OTT, A.; LAUTENSCHLÄGER, F. Oscillatory microrheology, creep compliance and stress relaxation of biological cells reveal strong correlations as probed by atomic force microscopy. **Frontiers in Physics**, v. 9, n. 711860, p. 1–12, 2021.

FUNG, Y. C. **Biomechanics**: mechanical properties of living tissues. New York: Springer, 1993. ISBN 978-038-79794-72.

GARROD, D.; CHIDGEY, M. Desmosome structure, composition and function. **Biochimica et Biophysica Acta**, Elsevier, v. 1778, n. 3, p. 572–587, 2008.

GREENWOOD, J. A.; MURPHY-ULLRICH, J. E. Signaling of de-adhesion in cellular regulation and motility. **Microscopy Research and Technique**, v. 43, n. 9858339, p. 420–432, 1998.

GUCK, J.; ANANTHAKRISHNAN, R.; MAHMOOD, H.; MOON, T. J.; CUNNINGHAM, C. C.; KÄS, J. The optical stretcher: a novel laser tool to micromanipulate cells. **Biophysical Journal**, v. 81, n. 2, p. 767–784, 2001.

HERTZ, H. **On the contact of rigid elastic solids and on hardness**. [S.l.]: Macmillan, 1882.

HOELZLE, D. J.; VARGHESE, B. A.; CHAN, C. K.; ROWAT, A. C. The optical stretcher: a microfluidic technique to probe cell deformability. **Journal of Visualized Experiments**, v. 1, n. 91, p. 1–10, 2014.

HOFFMAN, B. D.; CROCKER, J. C. Scaling cell mechanics: dissecting the physical responses of cells to force. **Annual Review of Biomedical Engineering**, v. 11, n. 1, p. 259–288, 2009.

HOFFMAN, B. D.; MASSIERA, G.; CITTERS, K. M. V.; CROCKER, J. C. The consensus mechanics of cultured mammalian cells. **Proceedings of the National Academy of Sciences**, v. 103, n. 27, p. 10259–10264, 2006.

HOOKE, R. **Micrographia**: or some physiological descriptions of minute bodies, made by magnifying glasses, with observations and inquiries thereupon. [S.l.]: London: Printed by John Martyn and James Allestry,, printers to the Royal Society, 1665.

KETENE, A. N.; SCHMELZ, E. M.; ROBERTS, P. C.; AGAH, M. The effects of cancer progression on the viscoelasticity of ovarian cell cytoskeleton structures. **Nanomedicine: Nanotechnology, Biology and Medicine**, Elsevier, v. 8, n. 1, p. 93–102, 2012. Available at: https://doi.org/10.1016/j.nano.2011.05.012.

KOLLMANNSBERGER, P.; FABRY, B. Linear and nonlinear rheology. **Annual Review of Materials Research**, v. 41, n. 1, p. 75–97, 2011.

KOLLMANNSBERGER, P.; MIERKE, C. T.; FABRY, B. Nonlinear viscoelasticity of adherent cells is controlled by cytoskeletal tension. **Soft Matter**, Royal Society of Chemistry (RSC), v. 7, n. 7, p. 3127–3132, 2011. Available at: https://doi.org/10.1039/c0sm00833h.

LAKES, R. S. **Viscoelastic Solids**. United Kingdom: CRC Press, 1998. ISBN 978-1138562899.

MALVERN, L. E. **Introduction to the Mechanics of a Continuous Medium**. Englewood Cliffs, NJ: Prentice-Hall, 1969. ISBN 978-0-13-487603-0.

MAO, Y.; NIELSEN, P.; ALI, J. Passive and active microrheology for biomedical systems. **Frontiers in Bioengineering and Biotechnology**, v. 10, n. 916354, p. 1–32, 2022.

MECHANOBIOLOGY INSTITUTE . **What steps are involved in Lamellipodia assembly?** National University of Singapore: MBINFO Defining Mechanobiology, 2018. Available at: https://www.mechanobio.info/cytoskeleton-dynamics/what-are-lamellipodia-and-lamella/what-steps-are-involved-in-lamellipodia-assembly/. Accessed on: 11 jun. 2023.

MIERKE, C. T. **Physics of Cancer**: interplay between tumor biology, inflamation and cell mechanics. [S.l.]: IOP Publishing, 2018. ISBN 978-0-7503-1753-5.

MOEENDARBARY, E.; HARRIS, A. R. Cell mechanics: principles, practices, and prospects. **Wiley Interdisciplinary Reviews: Systems Biology and Medicine**, v. 6, n. 5, p. 371–388, 2014.

MORALES, M. P.; GRABULOSA, M.; ALCARAZ, J.; MULLOL, J.; MAKSYM, G. N.; FREDBERG, J. J.; NAVAJAS, D. Measurement of cell microrheology by magnetic twisting cytometry with frequency domain demodulation. **Journal of Applied Physiology**, v. 91, n. 3, p. 1152–1159, 2001.

OLIVEIRA, D. A. A. P.; OLIVEIRA, R. F.; ZANGARO, R. A.; SOARES, C. P. Evaluation of low-level laser therapy of osteoblastic cells. **Photomedicine and Laser Surgery**, v. 26, n. 4, p. 401–404, 2008.

OMORI, T.; IMAI, Y.; KIKUCHI, K.; ISHIKAWA, T.; YAMAGUCHI, T. Hemodynamics in the microcirculation and in microfluidics. **Annals of Biomedical Engineering**, v. 43, n. 1, p. 238–257, 2014.

OTTO, O.; ROSENDAHL, P.; MIETKE, A.; GOLFIER, S.; HEROLD, C.; KLAUE, D.; GIRARDO, S.; PAGLIARA, S.; EKPENYONG, A.; JACOBI, A.; WOBUS, M.; TÖPFNER, N.; KEYSER, U. F.; MANSFELD, J.; FISCHER-FRIEDRICH, E.; GUCK, J. Real-time deformability cytometry: on-the-fly cell mechanical phenotyping. **Nature Methods**, v. 12, n. 3, p. 199–202, 2015.

PHAN-THIEN, N. **Understanding Viscoelasticity**: basics of rheology. [S.l.]: Springer-Verlag Berlin, Heidelberg, 2002. ISBN 978-3-662-10704-1.

REBELO, L. M.; SOUSA, J. S.; FILHO, J. M.; SCHÄPE, J.; DOSCHKE, H.; RADMACHER, M. Microrheology of cells with magnetic force modulation atomic force microscopy. **Soft Matter**, v. 10, n. 13, p. 2141–2149, 2014.

REINER, M. The deborah number. **Physics Today**, v. 17, n. 1, p. 62, 1964.

RIGATO, A.; MIYAGI, A.; SCHEURING, S.; RICO, F. High- frequency microrheology reveals cytoskeleton dynamics in living cells. **Nature Physics**, v. 13, p. 771, 2017.

SALAMEH, A.; DHEIN, S. Effects of mechanical forces and stretch on intercellular gap junction coupling. **Biochimica et Biophysica Acta (BBA)-Biomembranes**, v. 1828, n. 1, p. 147–156, 2013.

SANFORD, K. K.; EARLE, W. R.; LIKELY, G. D. The growth in vitro of single isolated tissue cells. **Journal of the National Cancer Institute**, v. 9, n. 3, p. 229–246, 1948.

SMITH, B. A.; TOLLOCZKO, B.; MARTIN, J. G.; GRÜTTER, P. Probing the viscoelastic behavior of cultured airway smooth muscle cells with atomic force microscopy: stiffening induced by contractile agonist. **Biophysical Journal**, v. 88, n. 4, p. 2994–3007, 2005.

SNEDDON, I. N. The relation between load and penetration in the axisymmetric boussinesq problem for a punch of arbitrary profile. **International Journal of Engineering Science**, Elsevier, v. 3, n. 1, p. 47–57, 1965.

SOUSA, J. S.; FREIRE, R. S.; SOUSA, F. D.; RADMACHER, M.; SILVA, A. F. B.; RAMOS, M. V.; MONTEIRO-MOREIRA, A. C. O.; MESQUITA, F. P.; MORAES, M. E. A.; MONTENEGRO, R. C.; OLIVEIRA, C. L. N. Double power-law viscoelastic relaxation of living cells encodes motility trends. **Scientific Reports**, Nature, v. 10, n. 4749, p. 363–378, 2020.

STAMENOVIĆ, D.; SUKI, B.; FABRY, B.; WANG, N.; FREDBERG, J. J. Rheology of airway smooth muscle cells is associated with cytoskeletal contractile stress. **Journal of Applied Physiology**, v. 96, n. 5, p. 1600–1605, 2004.

TAYLOR, J. R. **Mecânica Clássica**. [S.l.]: Bookman, 2013. ISBN 978-85-8260-087-0.

TSCHOEGL, N.; KNAUSS, W. G.; EMRI, I. Poisson's ratio in linear viscoelasticity–a critical review. **Mechanics of Time-Dependent Materials**, Kluwer Academic Publisher, v. 6, n. 1, p. 3–51, 2002.

WALKO, G.; CASTAÑÓN, M. J.; WICHE, G. Molecular architecture and function of the hemidesmosome. **Cell and Tissue Research**, Springer, v. 360, n. 3, p. 363–378, 2015.

ZANETTE, S. I. **Introdução à Microscopia de Força Atômica**. [S.l.]: Editora Livraria da Física, 2010. ISBN 978-85-7861-055-5.

ZHONG, M. C.; GONG, L.; LI, D.; ZHOU, J. H.; WANG, Z. Q.; LI, Y. M. Optical trapping of core-shell magnetic microparticles by cylindrical vector beams. **Applied Physics Letters**, v. 105, n. 18, p. 181112, 2014.

APPENDIX A – TABLES WITH MEASURED DATA

Table 3 – Medians of Young's modulus (Pa) corresponding to a force map (contact mode) for each L929 cell in cell culture obtained from the Hertz fit. In this case, the frequency is kept constant during the measurements, varying only the force exerted on the cell during indentation.

Index of cell measured	Frequency: 0.5 Hz				Frequency: 1.0 Hz			
	1 nN	2 nN	4 nN	8 nN	1 nN	2 nN	4 nN	8 nN
	E (Pa)				E (Pa)			
1	1225.00	2250.00	2720.00	4750.00	646.26	694.66	665.09	893.49
2	947.17	1320.00	1540.00	2680.00	1285.00	1410.00	1615.00	2125.00
3	1035.92	721.62	821.71	1220.00	1055.00	965.33	995.22	1410.00
4	691.69	647.93	1505.00	2445.00	565.21	624.66	735.30	1215.00
5	1380.00	1065.00	1175.00	1520.00	388.44	620.41	862.79	1345.00
6	937.41	1495.00	1880.00	1680.00	1070.00	1025.00	1300.00	1300.00
7	894.40	993.14	1035.00	1200.00	1120.00	1390.00	1590.00	1800.00
8	405.04	406.43	589.14	1440.00	1705.00	1950.00	1850.00	2040.00
9	2625.00	1910.00	1365.00	1435.00	1810.00	975.76	1295.00	2260.00
10	849.97	1125.00	1465.00	2260.00	985.39	736.23	794.48	1265.00
11	366.17	552.04	1090.00	1935.00	1070.00	1415.00	1495.00	1800.00
12	950.04	1021.38	1060.00	1175.00	1200.00	1450.00	1370.00	1660.00
14	1855.00	2040.00	1595.00	1865.00	3315.00	3625.00	3175.00	3145.00
13	1240.00	1225.00	1205.00	1365.00	2135.00	2765.00	5890.00	5620.00
15	835.46	713.72	1270.00	2030.00	1017.64	1200.00	1390.00	1440.00

Source: Created by the author.

Table 4 – Medians of Young's modulus (Pa) corresponding to a force map (contact mode) for each L929 cell in cell culture obtained from the Hertz fit. In this case, the force is kept constant at 2 nN during the measurements, varying only the oscillation frequency.

Index of cell measured	Force: 2nN			
	0.25 Hz	0.50 Hz	1.00 Hz	2.00 Hz
	E (Pa)			
1	744.03	1260.00	1175.00	1220.00
2	857.28	892.90	1215.00	1225.00
3	936.43	1040.65	1110.00	1145.00
4	554.97	729.45	835.01	825.19
5	344.11	367.01	426.02	419.86
6	1390.00	1155.00	507.24	387.40
7	893.56	1011.48	1120.00	1090.00
8	1020.00	1090.00	1055.00	1195.00
9	742.97	651.31	714.19	775.41
10	1980.00	1490.00	1835.00	2490.00
11	1079.86	1340.00	1360.00	1315.00
12	1495.00	1605.00	2120.00	2565.00
13	874.95	914.83	1064.10	1350.00

Source: Created by the author.